

26 Introduction

27 Cytoplasmic dynein is a motor protein essential for transporting nearly all intracellular
28 cargoes toward the minus end of microtubules (MTs) in most eukaryotes. Dynein's
29 cargoes include organelles, proteins, RNA, viruses, and vesicles¹. Additionally, dynein
30 plays key roles in other cellular processes such as mitosis and organelle positioning^{1,2}.
31 Mutations affecting dynein or its regulatory proteins have been linked to
32 neurodevelopmental and neurodegenerative diseases, including spinal muscular
33 atrophy (SMA), ALS, Huntington's disease, lissencephaly, and microcephaly³⁻⁹.

34 The 1.4 MDa dynein complex contains pairs of six subunits. The largest subunit is the
35 dynein heavy chain (DHC), which contains the N-terminal tail domain and C-terminal
36 motor domain. The tail domain facilitates dimer formation, recruits the dimers of
37 intermediate chain (DIC), light intermediate chain (DLIC), and interacts with dynactin,
38 cargo adaptors and other regulatory proteins¹⁰⁻¹³. The N-terminus of DIC (DIC-N)
39 recruits three pairs of light chains, Robl, LC8, and Tctex^{1,14,15}. DIC segments binding to
40 LC8 and Tctex, known as IC-LC tower, play a crucial role in assembling the dynein-
41 dynactin-adaptor (DDA) complex¹¹. The dynein motor domain belongs to AAA+
42 (ATPases Associated with diverse cellular Activities) protein families and consists of six
43 AAA subdomains (AAA1-6)^{16,17}. AAA1 is the primary subdomain that hydrolyzes ATP to
44 power dynein motility along MTs. The dynein motor domain attaches to MTs via the
45 coiled-coil stalk and the MT-binding domain (MTBD) and connects to the tail through the
46 linker domain located at the surface of the AAA+ ring¹⁷⁻²⁰.

47 Dynein alternates between two key conformational states: the autoinhibited Phi (similar
48 to the Greek letter "φ") and the open conformations^{14,21}. Phi dynein adopts a compact
49 structure that limits its interactions with MTs and dynactin, which serves to minimize
50 unnecessary ATP hydrolysis when motor protein is not engaged in active transport^{14,22}.
51 Opening of the Phi enables dynein to assemble with dynactin and the cargo adaptor,
52 allowing processive movement along MTs^{10,14}, a process supported by dynein
53 regulators Nde1/Ndel1 and Lis1^{3,15,23-30}. However, the underlying mechanism promoting
54 Phi to open transition is unclear.

55 Lis1, the first gene identified in relation to a neuronal migration disease, plays a crucial
56 role in dynein-related function^{3,11,31-39}. Lis1 possesses an N-terminal LisH domain that
57 facilitates dimerization and a C-terminal WD-40 β-propeller domain that binds to
58 Nde1/Ndel1, dynein, and other proteins³. Both domains are important at different stages
59 of dynein activation⁴⁰⁻⁴². The LisH domain interacts with dynactin p150 and DIC-N, thus
60 promoting the recruitment of dynactin and adaptors at the later stage of dynein
61 activation¹¹. WD-40 domains of Lis1 can directly bind to the dynein motor domain at the
62 AAA3-AAA4 sites (site-ring) and stalk coiled-coil (site-stalk)^{11,38,43}. Functional studies
63 proposed that Lis1 facilitates the formation of highly processive DDA complex by
64 favoring the release of Phi dynein and stabilizing open dynein^{34-37,44}. Lis1 binding is

65 thought to be incompatible with Phi dynein based on the steric clash when docking a
66 Lis1 β -propeller to the motor domains of Phi dynein^{3,35,37,44}. However, there is no direct
67 biochemical or structural evidence of whether Lis1 can open Phi dynein and
68 intermediary states that facilitate opening of Phi dynein remain unclear. A recent
69 structural study on tail-truncated yeast dynein motor domains reported a “Chi”
70 conformation, in which two Lis1 dimers are wedged between two AAA+ rings³⁷,
71 suggesting that two Lis1 dimers between the motor domains are required to crack open
72 Phi dynein. Furthermore, it is well-known that the AAA+ ring undergoes substantial
73 conformational changes under different nucleotide-binding states, which can potentially
74 regulate dynein–Lis1 binding. A more recent work has demonstrated that specific
75 nucleotide “codes” at the three variable nucleotide-binding sites (AAA1, 3, and 4)
76 govern the stoichiometry of dynein–Lis1 interactions by tuning their binding affinity at
77 two distinct locations⁴⁵. However, the intermediate structure for full-length human dynein
78 alone bound to Lis1 is still lacking and whether dynein forms a Chi conformation at the
79 initial state of its activation remains unclear.

80 Nde1 and its paralog Ndel1^{12,23}, are critical for all dynein-mediated functions in cell
81 division^{28,46}, cargo trafficking^{47,48} and neuronal migration^{49,50}. Nde1/Ndel1 is predicted to
82 be composed of the N-terminal coiled-coil domain and the C-terminal unstructured
83 region⁵¹⁻⁵³. The coiled-coil domain interacts with DIC-N, which overlaps with the DIC
84 binding site of the p150 subunit of dynactin^{52,54,55}. It also interacts with the WD-40
85 domains of Lis1, and its binding site on WD-40 domain overlaps with the Lis1 binding
86 site of dynein^{26,52}. The multi-protein interaction modes of Nde1/Ndel1, along with its
87 overlapping binding sites with other proteins, make the functional interpretation of
88 Nde1/Ndel1 elusive. It has been proposed that Nde1 tethers Lis1 to dynein^{12,26,56-58} and
89 promotes Lis1-mediated activation of dynein^{11,26} (**Fig. 1a**). According to this model, Phi
90 dynein first adopts an ‘open’ conformation. Lis1 stabilizes the open dynein by preventing
91 it from transitioning back to Phi, thus favoring the assembly of the DDA complex^{11,34,35,44}.
92 Consistent with this model, overexpression of Lis1 can rescue the deletion of
93 Nde1/Ndel1 in cells^{58,59} and Nde1/Ndel1-mediated recruitment of Lis1 to dynein
94 enhances DDA assembly in vitro²⁶. An alternative model suggests that Ndel1 negatively
95 regulates dynein activation by competing with p150 for DIC-N binding and by
96 sequestering Lis1 away from dynein⁵². Consequently, how Lis1 and Nde1/Ndel1 form a
97 complex with dynein and promote the opening of Phi dynein is not well understood.

98 To understand the mechanism by which Nde1/Ndel1 and Lis1 prime dynein for the DDA
99 assembly, we investigated how human Lis1 and Nde1 affect the conformational states
100 of full-length human dynein using biochemical reconstitution and electron microscopy.
101 We showed that Nde1 promotes the formation of the dynein-Lis1 complex. Using
102 negative-stain EM, we provide direct evidence that Lis1 or Nde1 alone has little effect
103 on the equilibrium between the Phi and open conformations of dynein, but Lis1 and

104 Nde1 together significantly bias the equilibrium toward the open conformation,
105 demonstrating that Nde1 acts like a molecular chaperone to promote Lis1-mediated
106 opening of dynein. Cryo-EM imaging of dynein-Lis1 in the presence or absence of Nde1
107 captures a new intermediate and rate-limiting state during the dynein activation process,
108 characterized by a single Lis1 dimer binding between the motor domains of Phi dynein.
109 Lis1 binding to Phi dynein causes the rotation between two motor domains to relieve the
110 steric clash, forming a Phi-like dynein and Lis1 complex, named “Phi^L-Lis1”. While Lis1
111 binds to one of the motor domains through its canonical interaction sites, it also forms
112 new interfaces between the other motor domain at the AAA5, AAA6, and linker regions.
113 Mutagenesis at the novel interfaces together with single molecule motility assays
114 supported the critical role of this Phi^L-Lis1 during the dynein activation process.
115 Collectively, our findings shed light on the roles of Nde1 and Lis1 in the dynein
116 activation pathway.

117 **Results**

118 **Nde1 promotes Lis1 binding to Phi dynein and cooperatively releases dynein** 119 **autoinhibition**

120 To determine whether Nde1 promotes Lis1 binding to dynein, we performed mass
121 photometry (MP) assays to assess the Lis1 and Nde1 binding to full-length human
122 dynein under different conditions. In the absence of Nde1, Lis1 alone exhibited an
123 increased binding to dynein in a time-dependent manner, with the formation of a 37%
124 1:1 dynein:Lis1 (DL) complex within 60 minutes. The inclusion of Nde1 significantly
125 enhanced the dynein-Lis1 binding (69% of complex formation) in less than a minute,
126 consistent with Nde1/Ndel1-mediated tethering of Lis1 to dynein^{12,26,57} (**Fig. 1b**). To
127 further test if Nde1 preferentially recruits Lis1 to Phi or open conformation, we
128 performed these assays using the Phi mutant of dynein¹⁴ that only forms open
129 conformation. Lis1 was readily bound to open dynein, but the addition of Nde1 did not
130 further enhance Lis1 binding to dynein (**Extended Data Fig.1**), suggesting that Nde1 is
131 required for Lis1 recruitment to Phi dynein. These results are also consistent with the
132 previous observation that the Nde1 addition does not further enhance Lis1-mediated
133 activation of DDA complexes assembled with the Phi dynein mutant²⁶. Interestingly, the
134 formation of the dynein-Lis1-Nde1 tripartite complex was not observed (**Fig. 1b and**
135 **Extended Data Fig.1**), regardless of different nucleotide conditions (**Extended Data**
136 **Fig. 2**). Although previous reports indicated that Nde1 can interact with DIC-N in single
137 molecule imaging^{12,26} and pull-down assays^{26,52}, we also did not detect the dynein-Nde1
138 complex (**Fig. 1b, and Extended Data Fig. 2**), suggesting that Nde1 rapidly dissociates
139 from the complex after handing off Lis1 to dynein¹².

140 To determine whether Nde1-mediated Lis1 recruitment to dynein shifts the equilibrium
141 between Phi and open conformations, we used the negative stain EM imaging¹⁴ to

142 quantify the ratio of Phi dynein in the presence and absence of Lis1 and Nde1.
143 Specifically, we used freshly prepared dynein with ~50% of motors forming the Phi and
144 then incubated dynein with Lis1 and Nde1 (**Fig. 1c and Extended Data Fig. 3**) in the
145 presence of ATP. We found that Lis1 or Nde1 alone does not change the Phi ratio
146 compared with the control (**Fig. 1d-e**). However, the Phi ratio decreased 44% when we
147 incubated dynein with both Lis1 and Nde1 at a ratio of 1:2:2 (**Fig. 1d-e**). Collectively,
148 our results demonstrate that Nde1 specifically promotes Lis1 binding to Phi dynein and
149 facilitates opening of this autoinhibited conformation.

150 **A novel Phi^L-Lis1 structure**

151 Our MP results suggest that there is a rate-limiting step of Lis1 binding to Phi dynein,
152 and this step can be significantly accelerated by the addition of Nde1 (**Fig. 1b**). We
153 used cryo-EM to capture the potential intermediate states to reveal the structural basis
154 of this process. We focused on the particles that form the autoinhibited dynein (**Fig. 2a,**
155 **b and Extended Data Fig. 4, 5**). In the absence of Nde1, we unexpectedly observed a
156 novel structure in which a Lis1 dimer is wedged between the two stacked motor rings of
157 Phi dynein. The dynein in this complex shows a compact conformation, similar to but
158 not the same as the previously reported Phi structure¹⁴ and we referred this complex as
159 the “Phi^L-Lis1” (**Fig. 2a, c and Supplementary Video 1**). Despite excess Lis1, nearly
160 half of Phi dynein does not bind to Lis1 (42.7% Phi vs. 57.3% Phi^L-Lis1) (**Fig. 2a**).
161 Notably, we did not observe the “Chi” (two Lis1s bound to dynein), suggesting that the
162 “Chi” conformation may be specific to yeast dynein or may form when truncated dynein
163 containing only the motor domains is used instead of full-length motor³⁷.

164 In the Phi^L-Lis1 structure, Lis1 appears on the same side as the IC-LC tower of dynein
165 (front side), independent of the presence of Nde1 (**Fig. 2a, b**). Based on this structural
166 observation, along with previous evidence indicating that DIC-N can bind to both Lis1¹¹
167 and Nde1¹², we speculate that the transient dynein-Lis1-Nde1 forms only on the IC-LC
168 tower side. Although we do not observe clear cryo-EM densities for the DIC-N, it is
169 possible that the DIC-N can weakly interact with Lis1, thus recruiting Lis1 to the front
170 side of dynein.

171 Previous results suggest Lis1 can affect dynein's mechanochemical cycle and
172 nucleotide state^{11,60,61}. The high-resolution structure of the motor domain enabled us to
173 identify and compare the nucleotide states of the motor domains in Phi and Phi^L-Lis1
174 structures. Specifically, we found that AAA1 pockets of both motor domains exhibit the
175 same ADP-Mg²⁺ density (**Extended Data Fig.6a, b**), accompanied by a flexible sensor-I
176 loop, indicating the intermediate state of Pi releasing (**Extended Data Fig. 6c, d**).
177 Similarly, AAA3 pockets show clear ADP binding (**Extended Data Fig.6a, b**), indicating
178 that Lis1 binding does not influence the nucleotide states of the motor domains of
179 autoinhibited dynein.

180 We next premixed equimolar Nde1 and Lis1, then added dynein to achieve a final 1:2:2
181 ratio of dynein:Lis1:Nde1 (**Fig. 2b**). Strikingly, we obtained a similar Phi^{L} -Lis1 structure,
182 but no longer observed the Phi dynein alone in the presence of Nde1 (**Fig. 2a, b and**
183 **Supplementary Video 1**). This is consistent with the MP analysis showing that Nde1
184 instantly promotes Lis1 binding to dynein (**Fig. 1b**) and forming Phi^{L} -Lis1. These results
185 suggest that Phi^{L} -Lis1 formation is a rate-limiting intermediate state before dynein
186 opening. Remarkably, none of the 3D classes shows clear Nde1 density in Phi^{L} -Lis1,
187 suggesting that Nde1 is not part of this complex.

188 We also analyzed individual motor domains of open dynein and did not observe an
189 increase in the propensity of the dynein-Lis1 complex compared to open dynein alone in
190 the presence of Nde1 (**Extended Data Fig. 7**). Consistent with MP of the Phi dynein
191 mutant¹⁴ (**Extended Data Fig. 1**), these results show that Nde1 promotes Lis1 binding
192 to Phi dynein to form Phi^{L} -Lis1, whereas Lis1 can readily bind to open dynein and does
193 not require Nde1.

194 **Lis1 induces a relative rotation in the Phi conformation to accommodate its** 195 **binding**

196 Consistent with previous reports^{35,37,44}, our structural analysis reveals a severe steric
197 clash between Lis1 and Phi motor domain A (**Fig. 3a**) and this needs to be relieved to
198 accommodate Lis1's binding in Phi^{L} -Lis1 (**Fig. 3b**). Comparing Phi to Phi^{L} -Lis1 reveals a
199 relative rotation between the two motor domains, which results in the groove on the
200 front side of dynein becoming larger than the corresponding groove on the back side
201 (**Fig. 3c, d**). The enlarged groove on the front side allows Lis1 to fit between Phi^{L} motor
202 domains. However, docking of Lis1 to the back side with a smaller groove shows severe
203 clashes, explaining why there is only one Lis1 present in Phi^{L} -Lis1 (**Fig. 3e**). The
204 rotation between the motor domains in Phi^{L} -Lis1 also causes a slight anticlockwise twist
205 in the neck region (**Fig. 3d**). This twist likely promotes the unwinding of the tail,
206 generating a trend toward an open conformation of dynein. We concluded that Lis1
207 binding induces a rotation of Phi dynein motor domains to avoid steric clash with Lis1
208 (**Fig. 3 and Supplementary Video 1**).

209 **Novel interactions identified in Phi^{L} -Lis1**

210 In Phi^{L} -Lis1, WD-40 domains of Lis1 interact with both motor domains of dynein (MD-A
211 and MD-B). While Lis1 interacts with MD-B through its canonical interaction sites at the
212 AAA3, AAA4, and AAA5 regions^{38,43,62}, we observed previously uncharacterized
213 interaction sites of Lis1 with the linker, AAA6, and AAA5 regions of MD-A (**Fig. 4a,**
214 **Extended Data Fig. 8 and Supplementary Video 1**). Sequence alignment of Lis1
215 homologs shows that MD-A and Lis1 interface is highly conserved among higher
216 eukaryotes but less conserved in yeast (**Extended Data Fig. 9**), suggesting different
217 regulatory roles of Lis1 between higher eukaryotes and yeast. Structural comparison

218 indicates that two motor domains in Phi^{L} -Lis1 adopt an almost identical conformation.
219 The root-mean-squared-displacement of alpha carbon atoms ($\text{C}\alpha$ -RMSD) of the two
220 motor domains was 0.513 Å (**Fig. 4b**). Additionally, the MD-B bound with Lis1_{ring} and
221 Lis1_{stalk} in our results also shows no significant difference from the structure of Lis1
222 bound to the human dynein motor domain³⁸ ($\text{C}\alpha$ -RMSD: 0.868 Å) (**Fig. 4c**), suggesting
223 Lis1 binding does not induce structural changes within an individual motor domain.

224 The interactions between MD-A and Lis1_{ring} are notably compact (**Fig. 4a and**
225 **Extended Data Fig. 8**). The WD-40 domain of Lis1 interacts with dynein MD-A at
226 regions distributed across the linker, AAA6, and AAA5 region (**Fig. 4d-f**). Specifically, at
227 the linker-Lis1 binding site, the side chains of M329 and E300 of Lis1 engage in
228 hydrophobic and polar interactions with the side chains of V1563, P1562 and H1559 of
229 dynein. Additionally, K303 and S304, located on the flexible loop of the Lis1 WD-40
230 surface, interact with R1621, D1556, and E1622 of linker region (**Fig. 4d, Extended**
231 **Data Fig. 8a**).

232 Within the AAA6 interaction region, the interface is characterized by polar interactions
233 involving N203, D205, and Q222 of the Lis1 WD-40 domain and K4089, N4085, Q4117,
234 and S4115 of MD-A. The side chain of K4089 forms a salt bridge with the side chain of
235 D205 and establishes a hydrogen bond with the oxygen atom in the main chain of N203.
236 Q222 and D205 of Lis1 also form polar interactions with S4115 and Q4117 and N4085
237 residues of dynein (**Fig. 4e, Extended Data Fig. 8b**).

238 The AAA5-Lis1_{ring} WD-40 interface shows a more compact interaction (**Fig. 4f**). This
239 interface is mainly composed of residues Q3636, S3613, T3612, D3616, D3617, A3618,
240 and K3621 of dynein MD-A and Y225, C226, G190, H191, M172, and D192 of the Lis1
241 WD-40 domain (**Fig. 4f and Extended Data Fig. 8b**). Notably, the side chain of Y225 of
242 Lis1 forms a polar interaction with the side chain of Q3636. Additionally, the side chain
243 of D3616 and the main chain of D3617 form hydrogen bonds with the main chain of
244 C226. The side chain of A3618 forms hydrophobic interaction with the main chain of
245 G190, while residues M172 and H191 of Lis1 form hydrophobic and hydrophilic
246 interactions with the side chain of K3621. Additionally, novel interactions are formed
247 between MD-A and MD-B in the Phi^{L} -Lis1, compared with canonical Phi (**Extended**
248 **Data Fig. 10**), suggesting that the dynein Phi^{L} -Lis1 is a stable conformation.

249 **The Phi^{L} -Lis1 interface regulates Nde1-dependent dynein activation**

250 To evaluate whether the new interaction sites we detected between Lis1 and dynein
251 MD-A in Phi^{L} -Lis1 are critical for activation of dynein, we introduced three sets of Lis1
252 mutations targeting the interfaces that interact with the linker, AAA6, and AAA5 of
253 dynein. Key residues of Lis1_{ring} at each interface were mutated to charged residues or
254 alanine to disrupt these interactions (Lis1^{linker}: E300K, K303E, S304R and M329A;
255 Lis1^{AAA6}: N203K, D205K and Q222A; Lis1^{AAA5}: M172K, D192K, Y225A, C226D). Similar

256 to wild-type Lis1 (WT Lis1), these Lis1 mutants formed homodimers and interacted with
257 Nde1 (**Fig. 4g**). However, the binding efficiency of Nde1 was reduced for the Lis1^{AAA5}
258 mutant (**Fig. 4g**), suggesting that the AAA5-Lis1_{ring} interface may share a region
259 involved in Nde1 binding to Lis1 (**Extended Data Fig. 11**). The Lis1 mutants also bound
260 to dynein, and the dynein binding efficiency of Lis1 was increased with Nde1 (**Fig. 4h**).
261 Notably, we detected a mass population corresponding to dynein bound to one Nde1
262 and two Lis1^{AAA6} mutants, indicating that mutations to the AAA6 interaction site of Lis1
263 prevent dissociation of Nde1 from the dynein-Lis1 complex (**Fig. 4h**).

264 To determine how these mutations affect activation of dynein motility, we assayed
265 single molecule motility of complexes assembled with wild type dynein, dynactin, and
266 the BicDR1 adaptor (DDR) on surface-immobilized MTs in vitro in the presence and
267 absence of Lis1 and Nde1. Consistent with our previous observations²⁶, Lis1 enhanced
268 the run frequency of DDR about 3-fold, and Nde1 and Lis1 together increased the run
269 frequency 15-fold (**Fig. 4i, j and Supplementary Video 2**). In the absence of Nde1,
270 Lis1 mutants activated dynein motility at similar levels of WT Lis1. In the presence of
271 Nde1, Lis1^{linker} and Lis1^{AAA5} triggered activation of DDR motility similar to WT Lis1 (**Fig.**
272 **4i, j**). In comparison, Nde1 failed to enhance Lis1^{AAA6}-mediated dynein motility,
273 suggesting that Lis1^{AAA6} cannot form the stable Phi^L-Lis1 complex and open the Phi
274 conformation (**Fig. 4i, j**). Together with MP results, we demonstrate that mutations in
275 the Lis1^{AAA6} interface disrupt Nde1-mediated opening of the Phi conformation by Lis1,
276 highlighting the importance of the Phi^L-Lis1 structure in the dynein activation pathway.

277 Discussion

278 In this study, we investigated the structure and mechanism of how Lis1 and Nde1
279 rescue dynein from autoinhibition prior to the assembly of active dynein transport
280 machinery. Using negative stain EM imaging, we directly showed that Nde1 and Lis1
281 cooperatively promote the opening of Phi dynein, whereas neither Nde1 nor Lis1 alone
282 exhibited a significant effect on Phi opening (**Fig. 1c-e**). Lis1 can readily bind to open
283 dynein (**Extended Data Fig. 1**) and facilitate the assembly of DDA complexes and Nde1
284 addition does not further enhance DDA motility²⁶. Despite that Lis1 alone can bind to the
285 Phi dynein and potentially open this autoinhibited conformation⁴⁵, we show that Nde1
286 facilitates Lis1 to dock onto Phi dynein more efficiently and promote its switch it to the
287 open state before DDA assembly in this work. Similar to molecular chaperones, Nde1
288 rapidly dissociates from dynein after handing off Lis1, promoting dynein-Lis1 complex
289 formation but not existing in the final complex. Because Nde1 has an overlapping
290 binding site with the p150 subunit of dynactin on DIC-N¹², dissociation of Nde1 from
291 DIC-N after tethering Lis1 to dynein may enable efficient recruitment of dynactin to
292 dynein-Lis1 complexes.

293 Our structural and functional studies of dynein-Lis1 complexes revealed a key
294 intermediate step on Lis1 and Nde1 mediated opening of dynein. Although a dynein
295 dimer contains Lis1 binding sites on each motor domain, our MP assays showed that
296 Phi dynein recruits a single Lis1. Using cryo-EM imaging, we revealed a Phi^L-Lis1
297 structure in which the two AAA+ rings of Phi dynein rotate slightly backward to
298 accommodate Lis1 binding to the front side. This rotational motion reduces the spacing
299 between the AAA+ rings, thereby preventing Lis1 binding to the back side. Preferential
300 binding of Lis1 to the front side may be due to the IC-LC tower, which is located at the
301 front side of the Phi motor.

302 The Phi^L-Lis1 is fundamentally distinct from the previously reported Chi of yeast dynein
303 monomers³⁷. The Chi is stabilized by two Lis1, one on each side, and adopts a more
304 open and extended conformation compared to the Phi^L-Lis1 motor domains (**Extended**
305 **Data Fig. 12**). In comparison, our study utilized full-length, wild-type human dynein and
306 we could not detect Chi dynein even when we used this conformation as a reference
307 during cryo-EM image processing. It is possible that isolated dynein motor domains may
308 prefer to recruit two Lis1s and form more extended Chi. In comparison, full-length
309 dynein readily forms the compact Phi and structural constraints imposed by the tail
310 domain may restrict the relative movement of the Phi motor domains. Lis1 binding to the
311 front side of Phi^L dynein reduces the spacing on the back side, thereby preventing the
312 formation of Chi. Most interaction sites located at Lis1_{ring} surface of Chi-Lis1 are also
313 present in that of Phi^L-Lis1 (**Extended Data Fig. 9**). In comparison, Phi^L-Lis1 exhibits
314 more compact interactions (**Fig 4 and Extended Data Fig. 8,10**). Consistent with
315 Phi^L-Lis1, we did not detect complexes with one dynein and two Lis1s in MP,
316 suggesting that Phi^L-Lis1, rather than Chi, is the stable intermediate of full-length human
317 dynein.

318 The mutagenesis of the interactions between Lis1 and the AAA6 subdomain of MD-A in
319 Phi^L-Lis1 disrupts Nde1's ability to promote Lis1-mediated dynein activation, confirming
320 that the Phi^L-Lis1 is a key intermediate in the dynein activation pathway. However,
321 these mutations did not disrupt the mutant Lis1's ability to increase the run frequency of
322 dynein several-fold on its own. This is because WT dynein can be either in open or Phi
323 conformations with near equal probability in our conditions. Our model predicts that
324 mutant Lis1 can still bind and enhance DDA assembly of open dynein without Nde1.
325 However, it cannot further enhance dynein motility synergistically with Nde1 because
326 this mutant is deficient in forming Phi^L-Lis1.

327 Based on our results and previous observations, we propose a mechanism underlying
328 dynein activation by Lis1 and Nde1. In the absence of Nde1, Lis1 alone can bind to both
329 DIC-N and dynein motor domains¹¹, inducing a conformational change from canonical
330 Phi to Phi^L. However, the efficiency of this process is low and Lis1 cannot open Phi^L
331 dynein on its own (**Fig.1c-e, 2a**). In the presence of Nde1, Lis1-Nde1 is initially recruited

332 to DIC-N positioned at the front side of Phi dynein, facilitating more efficient binding of
333 Lis1 to the front side of Phi. The local enhancement of Lis1 near the Phi motor by Nde1
334 facilitates more efficient binding of Lis1 to Phi dynein (**Fig. 5 step-i, -ii**). Nde1 and Lis1
335 form a transient $\text{Phi}^{\text{L}}\text{-Lis1-Nde1}$ complex (**Fig. 5 step-i**). Nde1 dissociates
336 spontaneously, leading to $\text{Phi}^{\text{L}}\text{-Lis1}$ formation (**Fig. 5 step-ii**). Lis1 binding induces a
337 slight backward rotation of the two motor rings in $\text{Phi}^{\text{L}}\text{-Lis1}$ (**Fig. 3c**), suggesting an
338 intermediate state prior to an open state. Additionally, a slight twist in the neck region,
339 caused by motors rotation and likely inducing an unwinding trend in the tail, may also
340 contribute to dynein opening (**Fig. 3d**). Subsequently, $\text{Phi}^{\text{L}}\text{-Lis1}$ transitions to open
341 dynein-Lis1 with the assistance of Nde1 (**Fig. 5 step-iii**). The binding of Lis1 to dynein
342 facilitates DDA assembly and activates dynein motility by recruiting the p150 subunit of
343 dynactin to dynein through its LisH domain¹¹ (**Fig. 5, step-iv**). Future studies are
344 required to understand how Nde1 hands off Lis1 to dynein and why it rapidly dissociates
345 from dynein. In addition to its tethering role and facilitating the formation of $\text{Phi}^{\text{L}}\text{-Lis1}$, it
346 remains to be determined whether Nde1 has additional roles in helping Lis1 convert
347 $\text{Phi}^{\text{L}}\text{-Lis1}$ to the open dynein.

348 **Methods**

349 **Cloning and expression**

350 The plasmid encoding full-length human dynein⁶³ was generously provided by Andrew
351 Carter (His-ZZ-TEV-SNAPf DHC1_IC2C_LIC2_Tctex1_Rob11_LC8, Addgene plasmid
352 #111903). The His-ZZ-TEV-SNAPf tag is fused to the N-terminus of the dynein heavy
353 chain. Human Lis1 and Nde1 (residues N-terminal 1-190 residues, which functions
354 similarly to full-length Nde1 in the single motility assay²⁶), and the mouse BIDCR1 gene,
355 were each cloned individually into the pOmniBac backbone. The constructs featured a
356 ZZ-TEV tag at the N-terminus and a SNAPf tag at the C-terminus. Lis1 mutants
357 containing point mutations were generated using purchased DNA fragments (IDT)
358 containing the mutations and inserted into the plasmid backbone. The mutations were
359 verified by Oxford Nanopore full-plasmid sequencing. The constructs used in this study
360 are listed in **Supplementary Table 1**.

361 These proteins were all expressed in insect sf9 cells, as describe previously^{14,19,26} with
362 slight modifications. Briefly, Bacmid DNA isolated from the from DH10MultiBac
363 competent cells (Geneva Biotech) were transfected into the in sf9 insect cells with the
364 Cellfectin® II (Gibco) reagent. Protein expression in sf9 cells was accomplished by
365 infecting them with P2 virus at a cell density of 2.5 million cells/mL. For dynein
366 expression, 28 mL of P2 virus was added into a 1.4 L culture of sf9 cells. For Lis1, Nde1,
367 and BicDR1, 7 mL P2 virus was used to infect the 0.7 L sf9 cells. Cells were harvested
368 after 75 hours by centrifugation at 1000 rcf for 15 minutes at 4°C. The cell pellets were
369 flash-frozen in liquid nitrogen and stored at -80°C.

370 **Protein purification**

371 Purification for full-length human dynein was previous described¹⁹. Briefly, the cell
372 pellets from a 1.4 L cell culture were resuspended in 100 mL lysis buffer (50 mM
373 HEPES pH 7.2, 100 mM NaCl, 1 mM DTT, 0.1 mM ATP, 10% glycerol) containing 2
374 tablets of Complete EDTA-free protease inhibitor (Roche) and 2 mM PMSF. The
375 suspension was homogenized using a Dounce with a tight plunger for 15~25 strokes,
376 followed by clarification through centrifugation at 65,000 rpm with a Ti70 rotor (Beckman)
377 for 1 hour at 4°C. The supernatant was then incubated with 3 mL IgG Sepharose 6 fast
378 flow resin (Cytiva) for 3~4 hours on a roller at 4°C, followed by washed with 200 mL
379 lysis buffer and 200 mL TEV buffer (50 mM Tris-HCl pH 7.4, 150 mM K-acetate, 2 mM
380 Mg-acetate, 1 mM EGTA, 10% glycerol, 0.1 mM ATP, 1 mM DTT). Afterward, the resins
381 were incubated with TEV buffer supplemented with 400 ug TEV protease overnight at
382 4°C. The supernatant was collected and concentrated with a 100 kDa MWCO Amicon
383 concentrator, then loaded into a TSKgel G4000 column pre-equilibrated with the GF150
384 buffer (25 mM HEPES pH 7.2, 150 mM KCl, 1 mM MgCl₂, 5 mM DTT, 0.1 mM ATP).
385 Peak fractions were collected and concentrated to 2~3 mg/mL for Cryo-EM grid

386 preparation. The quality of the sample was evaluated with the SDS-PAGE gels and the
387 negative-stain EM.

388 The purification of Lis1, Nde1, and BicDR1 from a 0.7 L cell culture followed a similar
389 protocol to that of dynein, with a few modifications. Specifically, 50 mL of lysis buffer
390 was used to resuspend the cell pellets, and ATP was omitted from the GF150 buffer.
391 And Superose 6 Column (Cytiva) was used for size exclusion chromatography. The
392 concentrated proteins were aliquoted, flash-frozen in liquid nitrogen, and stored at -80°C.
393 The quality of the proteins was assessed using SDS-PAGE gels.

394 Dynactin was isolated from pig brains through a series of purification steps, including
395 SP Sepharose Fast Flow and MonoQ ion exchange chromatography (Cytiva), followed
396 by size exclusion chromatography using a TSKgel G4000SWXL column (Tosoh), as
397 described by previous protocol⁶⁴.

398 **MT reconstitution**

399 MTs were reconstituted using porcine tubulin, which was either purchased from
400 Cytoskeleton or purified in-house in MT buffer (25 mM MES, 70 mM NaCl, 1 mM MgCl₂,
401 1 mM EGTA, and 1 mM DTT, pH 6.5). The tubulin was concentrated to 10 mg/mL at
402 4°C, then flash-frozen and stored at -80°C. To polymerize the MTs, the tubulin was
403 diluted to 5 mg/mL in MT buffer supplemented with 3 mM GTP. The tubulin mixture was
404 incubated on ice for 5 minutes and then transferred to a 37°C incubator for 1 hour. After
405 incubation, the MTs were pelleted at 20,000 rcf for 8 minutes at room temperature and
406 resuspended in MT buffer supplemented with 5 μM paclitaxel before being stored at
407 room temperature.

408 **MP assay**

409 High-precision coverslips (Azer Scientific) were cleaned by alternating washes with
410 isopropanol and water three times in a bath sonicator, then air-dried. The gasket was
411 cleaned similarly, without sonication, and air-dried before being placed onto a clean
412 coverslip. A total of 14 μL of filtered mass photometry buffer (30 mM HEPES pH 7.4, 5
413 mM MgSO₄, 1 mM EGTA, and 10% glycerol) was added to a well for autofocus. The
414 protein sample was then applied to the well and diluted to a concentration of 5–20 nM in
415 the buffer. Protein contrast data were collected using a TwoMP mass photometer
416 (Refeyn 2) with two technical replicates. The instrument was calibrated with a standard
417 mix of conalbumin, aldolase, and thyroglobulin. MP profiles were analyzed by fitting to
418 multiple Gaussian peaks, with the mean, standard deviation, and percentages
419 calculated using DiscoverMP software (Refeyn). The data for parameters of a multi-
420 Gaussian fit of MP measurements is summarized in **Supplementary Table 2**.

421 **Negative-stain EM and data quantification**

422 Freshly purified dynein was diluted in GF150 buffer to a final concentration of 14.3 nM in
423 the presence of 0.1 mM ATP and subsequently evaluated using negative-stain electron
424 microscopy (EM). A 4 μ L aliquot of the sample was applied to glow-discharged carbon
425 film grids (Electron Microscopy Sciences) and stained with 2% uranyl acetate. The grids
426 were then imaged using a 120 kV Talos L120C electron microscope. Micrographs were
427 manually acquired at a magnification of 45,000x. More than 40 micrographs were
428 collected per experiment for each condition to obtain sufficient particles for statistical
429 analysis.

430 Samples for statistical analysis of the Phi ratio were prepared with the following molar
431 ratios: dynein: Lis1(dimer) at 1:0, 1:1, and 1:2; dynein: Nde1(dimer) at 1:0, 1:1 and 1:2;
432 dynein : Lis1 : Nde1 at 1:0:0, 1:1:1 and 1:2:2. The mixtures were incubated on ice for 90
433 minutes and subsequently subjected to negative staining. Each experimental group was
434 accompanied by its respective control. The assay was repeated independently three or
435 more times, using different batches of freshly purified protein.

436 Micrographs were processed using cryoSPARC, including blob picking, micrograph
437 extraction, and 2D classification. Briefly, micrographs from each experimental group
438 were merged, and particle picking was performed using templates of Phi and open
439 dynein. The particle diameter was set to 750 Å, and the distance cutoff for dynein
440 particles was 400 Å to optimize particle selection. All particles were extracted, followed
441 by three rounds of 2D classification. Phi and open dynein particles were identified from
442 the 2D classification and traced back to the corresponding micrographs for each
443 condition, where Phi and open particles were quantified. To calculate the normalized
444 fraction of Phi, the total number of Phi and paired open dynein particles was determined
445 for micrographs under a given condition. The ratio of Phi particles in the dynein-alone
446 condition ($N(\text{Phi}) / N(\text{Phi} + \text{open})$) was defined as proportion A, serving as the control for
447 each group. The ratio of Phi particles in each experimental condition, excluding the
448 dynein-alone control, was defined as proportion B ($N(\text{Phi}) / N(\text{Phi} + \text{open})$). The
449 normalized fraction of Phi was calculated as B/A, and GraphPad Prism was used to plot
450 the normalized fraction of Phi.

451 **Cryo-EM sample preparation**

452 For the dynein, Lis1, and Nde1 sample, Lis1 and Nde1 were incubated at a 1:1 molar
453 ratio for 30 minutes on ice. Freshly purified dynein, at a concentration of 2 mg/mL, was
454 then added to the Lis1-Nde1 complex at a 1:2:2 molar ratio and incubated on ice for 5
455 minutes, with 5 mM ATP added immediately prior to freezing. For the dynein and Lis1
456 complex, dynein (2 mg/mL) was incubated with Lis1 for 90 minutes on ice, and 5 mM
457 ATP was added just before vitrification.

458 For vitrification, 3.5 μ L of the prepared sample was applied to glow-discharged
459 Quantifoil holey carbon grids (R2/1, 300 mesh gold), which were treated for 45 seconds

460 at 25 mA using a GloQube Glow Discharge system (Quorum Technologies). The grids
461 were blotted for 2.5 to 4.5 seconds at 4°C and 100% humidity, then vitrified by plunging
462 into liquid ethane using a Vitrobot Mark IV (Thermo Fisher Scientific).

463 **Cryo-EM data collection**

464 Data were collected at the Yale ScienceHill Cryo-EM facility using a Glacios microscope
465 (Thermo Fisher Scientific) operated at 300 keV and equipped with a K3 detector. Data
466 collection was facilitated by SerialEM software, targeting a defocus range of -1.2 μm to -
467 2.6 μm . Four exposures per hole were recorded as movies, comprising 40 frames each,
468 with a total electron dose of 40 $\text{e}^-/\text{\AA}^2$. A total of 7,128 movies were collected for the
469 Dynein-Lis1-Nde1 condition, while 16,558 movies were collected for the Dynein-Lis1
470 condition.

471 **Cryo-EM data processing**

472 Cryo-EM movies were pre-processed using CryoSPARC Live, which included patch
473 motion correction and patch CTF estimation. The processing workflows are illustrated in
474 **Extended Data Fig. 4 and 5**. The statistics are summarized in **Table 1**.

475 For the dynein-Lis1 condition dataset, particles were picked using the blob picker,
476 extracted with a box size of 512 pixels, and downsampled to 128 pixels with a pixel size of
477 3.456 \AA . In total, 7,254,515 particles were extracted. The iterative 2D classification was
478 performed to filter the particles, resulting in the selection of 204,005 high-quality
479 particles for ab initio reconstruction. Initial maps for the dynein single motor domain and
480 the Phi^{L} -Lis1 motor domains were identified. The map of the Phi^{L} -Lis1 motor domains
481 was subsequently used for heterogeneous refinement of all original particles. The
482 original particles were divided into four subsets, each subjected to heterogeneous
483 refinement (4 classes). Three rounds of heterogeneous refinement were performed,
484 updating the reference each time, ultimately identifying the Phi and Phi^{L} -Lis1 motor
485 domains. The Phi and Phi^{L} -Lis1 motor domains were merged separately and extracted
486 from micrographs using a box size of 512 pixels, which was then binned to 384 pixels,
487 resulting in a pixel size of 1.1573 \AA . Two rounds of heterogeneous refinement were
488 conducted to exclude junk particles. High-quality subsets were selected for
489 homogeneous refinement, followed by two rounds of CTF refinement and local
490 refinement. The Phi^{L} -Lis1 motor domains achieved a resolution of 2.86 \AA , and the Phi
491 motor domains reached a resolution of 2.71 \AA , exhibiting C2 symmetry.

492 To reconstitute the tails of the Phi^{L} -Lis1 and Phi motor domains, the particles were
493 recentered at the tail and then extracted from micrographs using a box size of 512
494 pixels, binned to 256 pixels, yielding a pixel size of 1.736 $\text{\AA}/\text{px}$. Following this,
495 heterogeneous refinement was applied to filter the particles, and high-quality subsets
496 were selected for homogeneous refinement. The overall tail resolutions reached 4.21 \AA

497 for the Phi tail and 4.05 Å for the Phi^L-Lis1 tail. Four masks were devised to cover the
498 tail segments, which were divided into the NDD, left, right, and neck regions. Maps of
499 local refinement using these masks were integrated, referring to the consensus map of
500 the tail. The full-length map was assembled by stitching together the tail and motor
501 domains in ChimeraX, corresponding to Phi and Phi^L-Lis1, respectively.

502 For the Lis1-Nde1-dynein condition dataset, the process closely mirrored that of the
503 dynein-Lis1 condition described above. Briefly, the blob picker identified 2,393,279
504 particles. Following extraction from the micrographs and iterative 2D classification,
505 204,005 particles were selected for initial map generation through ab initio
506 reconstruction. An initial map for the Phi^L-Lis1 motor domains were obtained, which
507 were then subjected to iterative heterogeneous refinement using all particles with the
508 Phi^L-Lis1 initial map as a reference. However, the Phi motor domains did not appear in
509 the heterogeneous refinement, even when the verified Phi map from this study was
510 utilized as a reference. Subsequently, the Phi^L-Lis1 domain map was re-extracted from
511 the micrographs and underwent two rounds each of heterogeneous refinement, CTF
512 refinement, and local refinement, achieving a resolution of 2.88 Å. The consensus map
513 of the tail reached a resolution of 6.22 Å after recentering and re-extracting the tail
514 region. Masks and local refinement were employed to enhance the local resolution of
515 the tail. The full-length Phi^L-Lis1 structure was reconstituted by integrating the
516 composite tail map and motor map in ChimeraX.

517 **Model building and refinement**

518 For model building, previously reported structures 9BLY¹⁹, 9BLZ¹⁹, and 8FDT³⁸ were
519 utilized as the initial models for the full-length and motor domains of Phi and Phi^L-Lis1.
520 The individual domains, including the tail, single motor and Lis1 dimer, were extracted
521 from the 9BLY, 9BLZ, and 8FDT, and rigid-body fitting into the Cryo-EM maps were
522 performed using UCSF ChimeraX. The models were then manually constructed in
523 COOT^{65,66}, and followed by real-space refinement in Phenix⁶⁷. The quality of the refined
524 models was assessed using the MolProbity integrated into Phenix, with the statistics
525 reported in **Table 1**.

526 **Single-molecular motility assay**

527 Fluorescent imaging was conducted using a custom-built, multicolor objective-type TIRF
528 microscope based on a Nikon Ti-E microscope body. It was equipped with a 100X
529 magnification, 1.49 N.A. apochromatic oil-immersion objective (Nikon) and a Perfect
530 Focus System. Fluorescence signals were captured by an electron-multiplied charge-
531 coupled device camera (Andor, Ixon EM+, 512 × 512 pixels), with an effective pixel size
532 of 160 nm after magnification. Probes such as Alexa488/GFP/mNeonGreen, LD555,
533 and LD655 were excited by 488 nm, 561 nm, and 633 nm laser beams (Coherent),
534 coupled to a single-mode fiber (Oz Optics), and their emissions were filtered using

535 525/40, 585/40, and 697/75 bandpass filters (Semrock), respectively. The entire system
536 was controlled via MicroManager 1.4 software.

537 Biotin-PEG treated flow chambers were treated with 5 mg/ml streptavidin for 2 minutes,
538 followed by washing with MB buffer (30 mM HEPES pH 7.0, 5 mM MgSO₄, 1 mM EGTA,
539 1 mg/ml casein, 0.5% pluronic acid, 0.5 mM DTT, and 1 μM Taxol). Biotinylated MTs
540 were then added to the chamber for 2 minutes and washed again with MB buffer.
541 Proteins were prepared by diluting them to the desired concentrations in MB buffer. For
542 DDRNL complex assembly, a mixture of 10 nM dynein, 150 nM dynactin, 50 nM BicDR1,
543 200nM Lis1 and 10nM Nde1 was incubated on ice for 15 minutes, then diluted tenfold
544 into imaging buffer (MB buffer containing 0.1 mg/ml glucose oxidase, 0.02 mg/ml
545 catalase, 0.8% D-glucose, and 2 mM ATP) and introduced to the flow chamber. Motility
546 was observed and recorded for 40 seconds.

547 **Data analysis for single-molecular motility assay**

548 Single-molecule motility of the DDR complex was captured for 200 frames per imaging
549 area and analyzed as kymographs made in FIJI. Run frequency was determined by
550 counting the number of processive BicDR1 molecules on each MT, then dividing this
551 number by the MT length and the total data collection time, with a custom MATLAB
552 script. The p-values for the two-tailed Student's t-test were determined in Excel.

553 **Data availability**

554 Cryo-EM Density maps and models have been deposited in the Electron Microscopy
555 Data Bank and Protein Data Bank as follows: In the dynein and Lis1 condition: PDB-
556 XXX/EMD-XXX for full length Phi and PDB-XXX/EMD-XXX for motor domains of Phi;
557 PDB-XXX/EMD-XXX for full length Phi^L-Lis1 and PDB-XXX/EMD-XXX for motor
558 domains of Phi^L-Lis1. In the dynein, Lis1 and Nde1 condition: PDB-XXX/EMD-XXX for
559 full-length Phi^L-Lis1 and XXX/EMD-XXX for motor domains of Phi^L-Lis1.

560 **Acknowledgement**

561 We are very grateful to members of the Zhang and Yildiz laboratories for their valuable
562 discussions. This work was funded by the NIH/NIGMS (GM136414 to A.Y., and
563 GM142959 to K.Z.) and in part by a Collaboration Development Award Program (to K.Z.)
564 from the Pittsburgh Center for HIV Protein Interactions (U54AI170791). The Cryo-EM
565 data were collected at the Yale ScienceHill Cryo-EM facility. We would like to thank
566 Jianfeng Lin and Kaifeng Zhou for assistance with the data collection. Yale Cryo-EM
567 Resource is funded in part by the NIH grant S10OD023603 awarded to Frederick J.
568 Sigworth.

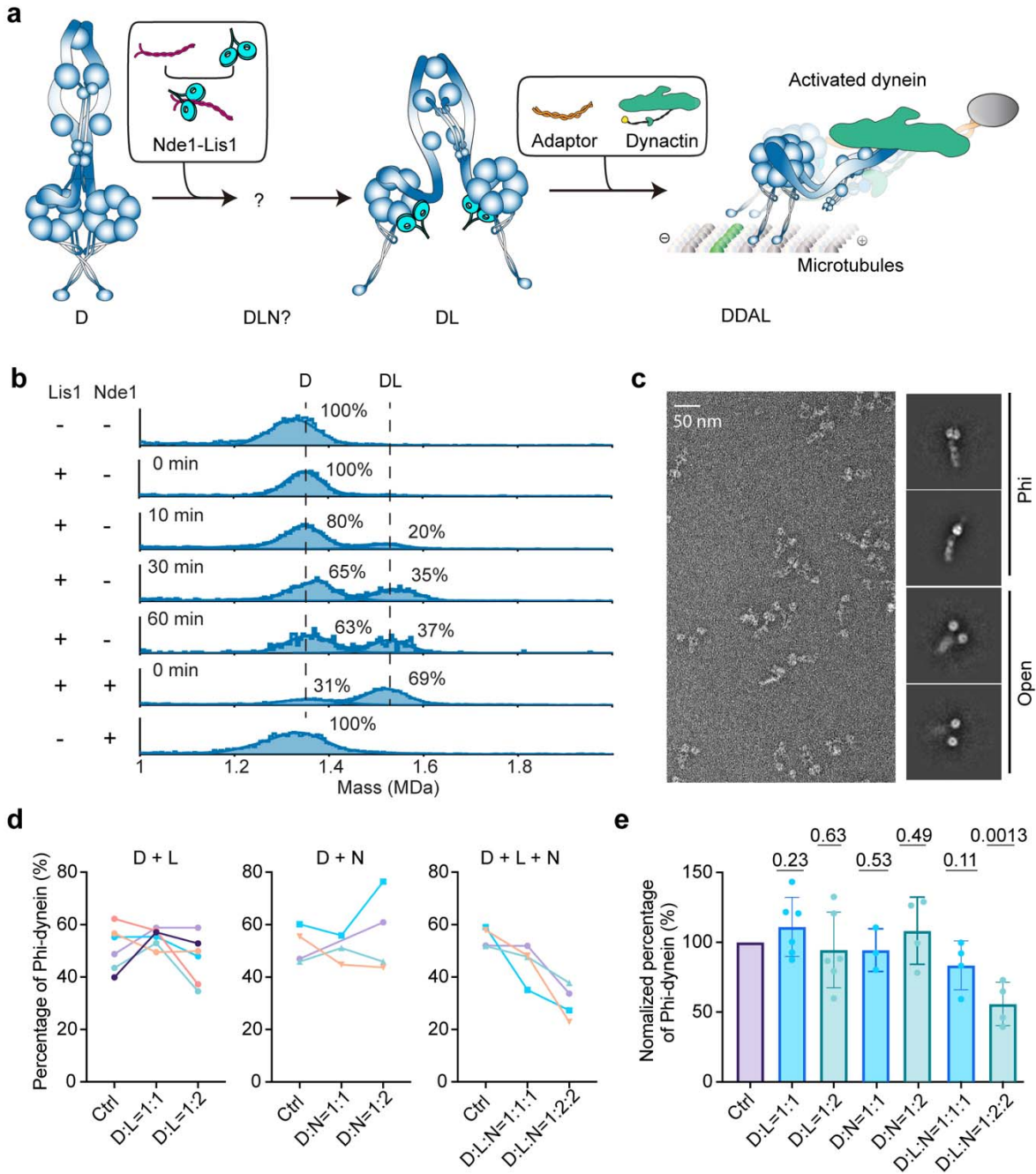
569 **Author contributions**

570 K.Z. and A.Z. designed the study. J.Y. expressed and purified dynein, Lis1 and Nde1
571 proteins for EM. J.Y. and P.C. prepared the cryo-EM samples, collected and processed
572 the data, and built the PDB models. P.C. and J.Y. processed negative stain EM data
573 and quantified the particle numbers. Y.Z. performed Lis1 mutagenesis, protein
574 preparation, TIRF and mass photometry assays. J.Y., P.C., Y.Z., K.Z., and A.Y.
575 analyzed the data and prepared figures. J.Y., Y.Z., P.C., K.Z., and A.Y. wrote the
576 manuscript with input from all authors.

577 **Competing Interests**

578 The authors declare no competing interests.

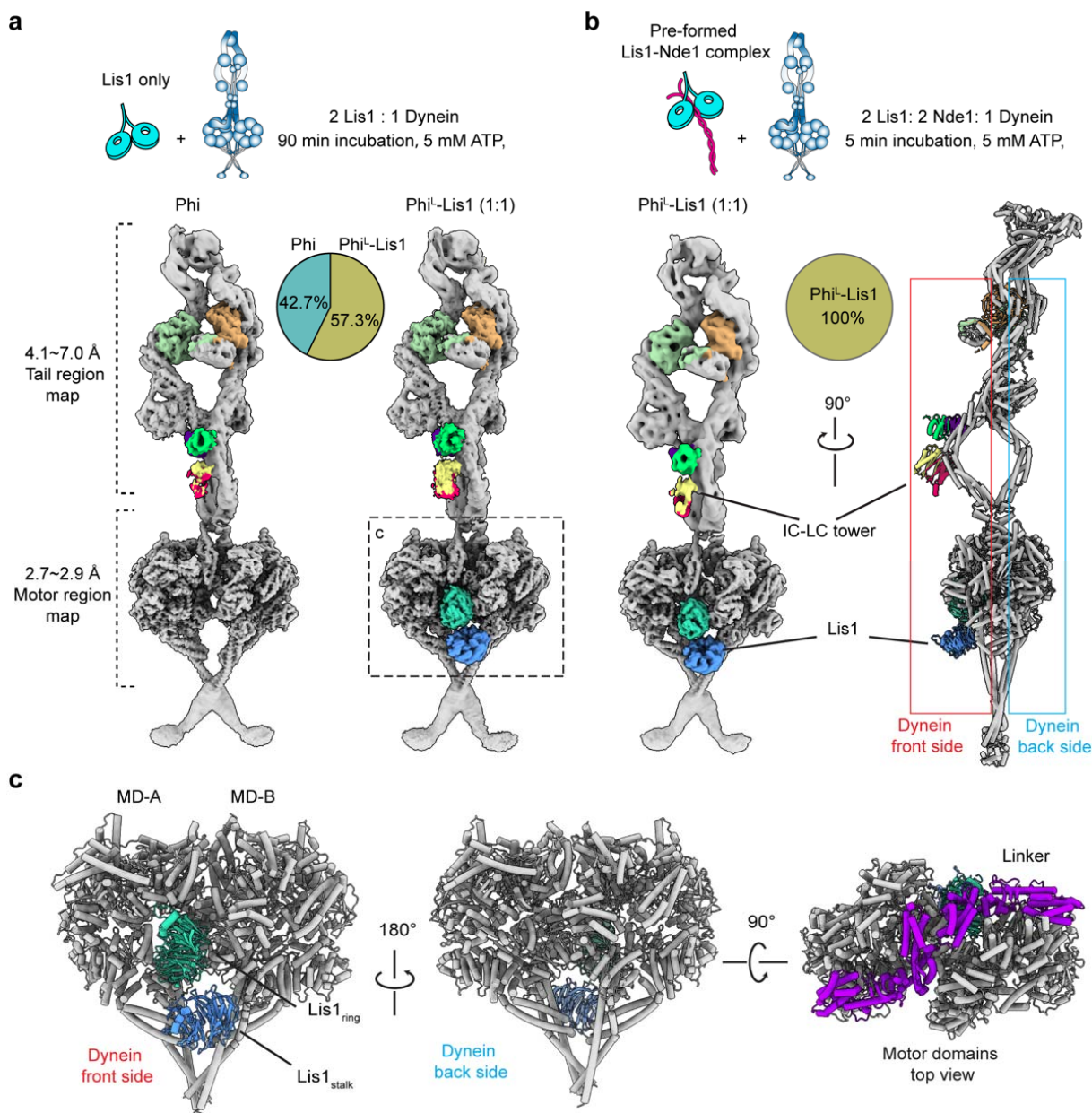
579 **Figures**



580

581 **Fig. 1. Nde1 promotes Lis1 binding to Phi dynein and cooperatively releases**
 582 **dynein autoinhibition.** **a**, Schematic of dynein activation. Nde1 tethers Lis1 to dynein
 583 and promotes Lis1-mediated formation of the active dynein-dynactin-adaptor-Lis1
 584 (DDAL) complex. Intermediate states between the association of Lis1-Nde1 and
 585 opening of dynein are unknown. **b**, MP shows that Lis1 alone slowly binds to dynein in

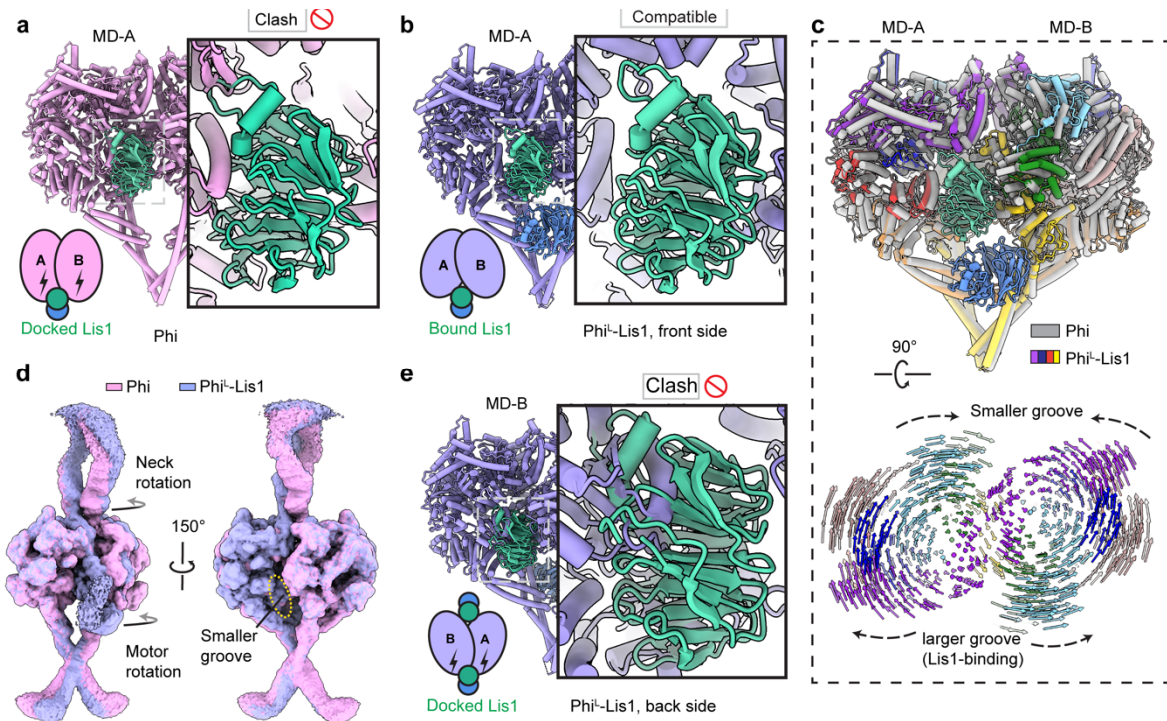
586 tens of minutes, whereas Nde1 promotes more rapid and efficient binding of Lis1 to
587 dynein. Dynein, Lis1 and Nde1 were included at a 1:2:2 ratio. Only one Lis1 dimer is
588 tethered to one dynein. Solid curves represent a fit to multiple Gaussians to predict the
589 average mass and percentage of each population. **c**, A representative image of dynein
590 motors captured using negative stain electron microscopy. Without Lis1 and Nde1,
591 dynein is distributed almost equally between Phi and open conformations. The
592 percentage of Phi was quantified after incubating dynein with Lis1, Nde1, or both
593 proteins for 90 min. The percentage of Phi (**d**) and the relative change of Phi (**e**) in the
594 presence and absence of Lis1 and Nde1 (mean \pm s.d.; from left to right, n=14, 6, 6, 3, 4,
595 4, 4 from three or more independent experiments). P values are calculated from a two-
596 tailed *t* test. The control (Ctrl) of panel e represents dynein alone from the three groups
597 of panel d (Ctrl) normalized to 100%.



598

599 **Fig. 2. The structure of Phi^L-Lis1 complex.** **a**, (Top) Full length human dynein was
600 incubated with Lis1 with a molar ratio of 1:2 on ice for 90 min before flash frozen.
601 (Bottom) Cryo-EM maps of Phi and Phi^L-Lis1 complex structures in front view and
602 percentages of particles with these two conformations (open dynein excluded). **b**, (Top)
603 Dynein was incubated with Lis1 and Nde1 with a molar ratio of 1:2:2 on ice for 5 min
604 before flash frozen. (Bottom) The structure of Phi^L-Lis1 obtained under this condition is
605 shown in front view and side view. All particles were classified into the Phi^L-Lis1
606 conformation and Phi conformation could not be detected. **c**, Model of the Phi^L-Lis1
607 motor domains is shown in three views. One Lis1 dimer is clamped between MD-A and
608 MD-B of Phi^L-Lis1 on the front side, while the back side of the motor domains is vacant,

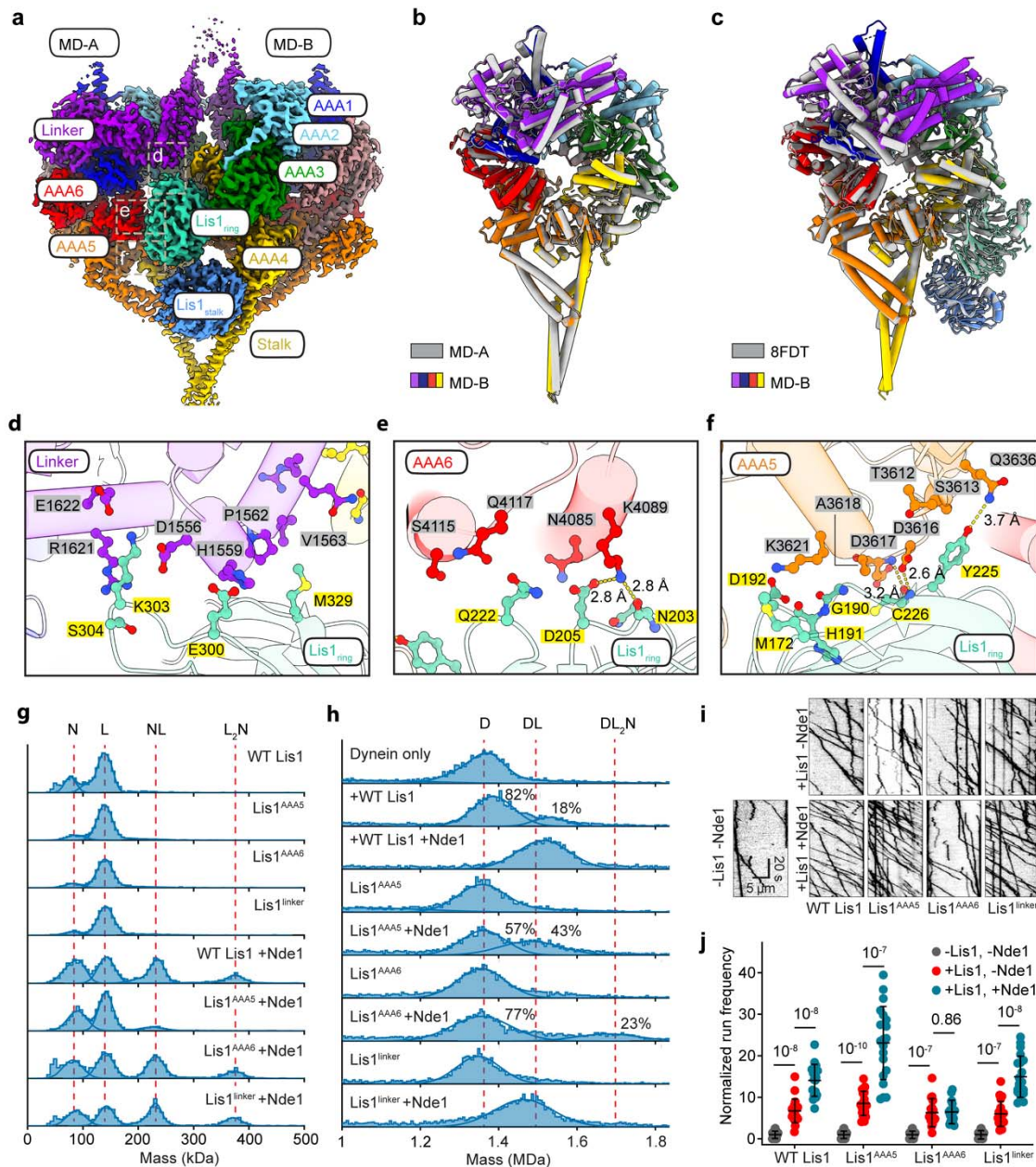
609 with no Lis1 bound. The top view reveals that the linker regions (purple) of MD-A and -B
610 interact with each other.



611

612 **Fig. 3. Lis1 induces a transition in the Phi conformation to accommodate its**
 613 **binding.** **a**, Docking of a Lis1 monomer between dynein motor rings shows a clash with
 614 the rigid canonical Phi MD-A. **b**, A Lis1 dimer bound to dynein motors on the front side
 615 is compatible with the coordinated Phi^L structure. **c**, (Top) The superimposition of the
 616 Phi and Phi^L-Lis1 motor domains. Phi and Phi^L-Lis1 are colored with grey and rainbow
 617 respectively. (Bottom) Comparison of the motor domains between Phi^L-Lis1 and
 618 canonical Phi. Lis1 is hidden for clarity. Vectors present interatomic distance of pairwise
 619 Cα atoms between the Phi to Phi^L-Lis1 structures. Lis1 binding induces a slight rotation
 620 of the dynein motor domains from the Lis1-bound (front) side toward the back, resulting
 621 in a larger groove at the front side compared to the smaller groove at the back. **d**,
 622 Overlay of the motor domain maps of Phi and Phi^L-Lis1 with MD-A aligned at a lower
 623 contour level. The rotation of Phi^L-Lis1 motor domain induces rotation in the neck region,
 624 showing a slight unwinding trend, which contributes to the formation of a smaller groove
 625 on the back side. **e**, Docked Lis1 on the back side of Phi^L-Lis1 causes a significant
 626 clash with MD-B.

627



628

629

630

631

632

633

634

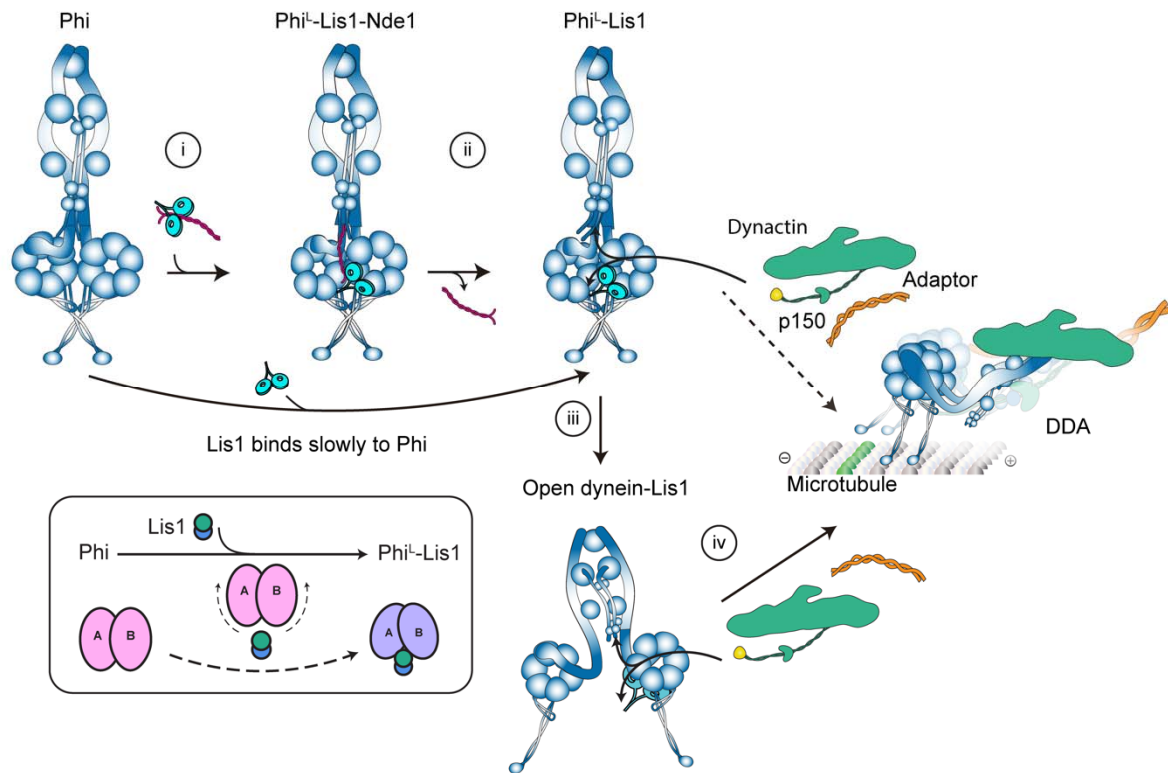
635

636

Fig. 4. Novel interactions identified between Lis1_{ring} and MD-A in Phi^L-Lis1. a, Cryo-EM density map highlighting the subdomains involved in the interface between Lis1 and the dynein motor. Lis1 and subdomains of MD-A and MD-B are colored separately. Novel interfaces between MD-A and Lis1_{ring} are marked by dash rectangle and enlarged in panels d, e, and f. **b,** Comparison of MD-A (grey) and -B (rainbow) of Phi^L-Lis1. **c,** Comparison of MD-B (rainbow) with the Lis1-bound structure of the motor domain of human dynein (PDB: 8FDT, grey). Representative interactions located at linker-Lis1_{ring} (**d**), AAA6-Lis1_{ring} (**e**), and AAA5-Lis1_{ring} (**f**) interface are shown with stick

637 mode, colored according to their respective subdomains. **g**, MP profiles illustrate the
638 interaction of Nde1 (N) with WT Lis1 (L) and Lis1 mutants (Lis1^{AAA5}, Lis1^{AAA6}, and
639 Lis1^{linker}). Nde1 interacts with one (NL) or two (NL₂) Lis1 dimers. Lis1^{AAA5} exhibits a
640 reduced binding percentage to Nde1. **h**. MP shows the binding of Lis1 mutants to
641 dynein with or without Nde1. Dynein, Lis1 and Nde1 were incubated for 2 minutes at
642 1:2:2 ratio (D: dynein only, DL: one dynein and one Lis1, DL₂N: one dynein, two Lis1,
643 and one Nde1). **i**, Representative kymographs show the motility of WT DDR complexes
644 with or without Nde1 and Lis1. **j**, Run frequency of WT DDR with or without Nde1 and
645 Lis1 (mean \pm s.d.; n = 20 MTs for each condition; statistics from two independent
646 experiments). Results were normalized to the -Lis1, -Nde1 condition.

647



648

649 **Fig. 5. Model for the initial stage of dynein activation by Nde1 and Lis1.**
 650 **Step-i,** Nde1 tethers Lis1 to Phi dynein and forms a transient $\text{Phi}^{\text{L-Lis1-Nde1}}$ complex.
 651 **Step-ii,** Nde1 dissociates spontaneously from dynein, leading to the formation of $\text{Phi}^{\text{L-Lis1}}$.
 652 Without Nde1, Lis1 binding to Phi dynein and formation of $\text{Phi}^{\text{L-Lis1}}$ becomes a less
 653 efficient and slow process. The binding of Lis1 induces a slight backward rotation of the
 654 two motor rings and a twist in the neck region, likely leading an unwinding trend in the
 655 tail and contributing to dynein opening. **Step-iii,** $\text{Phi}^{\text{L-Lis1}}$ transitions to open dynein-
 656 Lis1 assisted by Nde1. **Step-iv,** Lis1 promotes processive DDA complex assembly by
 657 interacting with p150 and DIC-N through its LisH domain. The dashed line indicates the
 658 possibility that Lis1 in the $\text{Phi}^{\text{L-Lis1}}$ complex promotes dynactin recruitment and DDA
 659 assembly without switching to the open conformation.

In dynein and Lis1 condition					In Nde1, Lis1 and dynein condition	
Description	Composite map of full-length Phi	Composite map of full-length Phi ^L -Lis1	Phi motor	Phi ^L -Lis1 motor	Composite map of full-length Phi ^L -Lis1	Phi ^L -Lis1 motor
PDB code	xxx	xxx	xxx	xxx	xxx	xxx
Data Collection and Processing						
Facility	Yale ScienceHill-Cryo-EM facility				Yale ScienceHill-Cryo-EM facility	
Microscope	Glacios				Glacios	
Voltage (kV)	200				200	
Camera	K3				K3	
Magnification	45k				45k	
Pixel Size (Å)	0.432 (super resolution)				0.432 (super resolution)	
Total Electron Exposure (e-/Å ²)	40				40	
Defocus Range (µm)	1.5-2.7				1.5-2.7	
Symmetry Imposed	C1	C1	C2	C1	C1	C1
Num of mics	16,558				7,128	
Initial Particles	7,254,515				2,393,279	
Final Particles	103,097	127,963	160,539	215,049	61,684	127,611
Refinement						
Initial models	9BLY ab initio	9BLY 8FDT ab initio	9BLZ ab initio	8FDT ab initio	9BLY 8FDT ab initio	8FDT ab initio
Map pixel size	1.7360	1.7360	1.1573	1.1573	1.736	1.157
Map Resolution (Å) (FSC 0.143)	4.50	4.50	2.71	2.86	5.0	2.88
Map sharpening B-factor (Å ²)	/	/	72.3	69.6	/	51.7
Model Composition						
Non-hydrogen atoms	89,388	94,497	47418	21,370	94,497	52,508
Protein residues	11,061	11,704	5784	6514	11,704	6,515
Ligands	MG:4 ATP:2 ADP:6	MG:4 ATP:2 ADP:6	MG:4 ATP:2 ADP:6	MG:4 ATP:2 ADP:6	MG:4 ATP:2 ADP:6	MG:4 ATP:2 ADP:6
Model vs. Data						
FSC Map to Model (Å) (FSC 0.5)	3.5	3.8	3.0	3.1	3.5	3.4
Correlation coefficient (mask)	0.60	0.59	0.86	0.87	0.51	0.84
B factors (Å²)						
Protein	117.05	112.65	14.13	38.69	260.48	52.33
Ligand	75.90	79.64	1.76	14.44	69.27	32.47
R.m.s deviation						
Bond length (Å)	0.006	0.004	0.003	0.003	0.002	0.002
Bond angles (°)	0.683	0.693	0.548	0.527	0.544	0.548
Validation						
Molprobrity score	1.87	1.88	1.40	1.41	1.75	1.45
Clashscore	13.26	13.07	7.31	7.33	10.62	8.06
Rotamer outliers (%)	0.00	0.00	0.00	0.00	0.00	0.02
Ramachandran plot						
Outliers (%)	0.09	0.07	0.00	0.00	0.05	0.00
Allowed (%)	3.52	3.74	1.50	2.05	3.23	2.05
Favored (%)	96.39	96.20	98.50	97.95	96.72	97.95
Rama-Z (whole)	0.62	0.53	1.60	1.72	0.92	1.86

660 Table 1. Cryo-EM data collection, refinement, and validation statistics.

Construct	Vector	Source	Figures
SNAPf-DYNH1C1-IC2C-LIC2-Robl1-Tctex1-LC8	pOmniBac-pIDC	Schlager et al., 2014	F1, 2, 3, 4, EDF2, 3, 4, 5, 6, 8, 9, 12
SNAPf-DYNH1C1 ^{R1567E, K1610E} -IC2CLIC2-Robl1-Tctex1-LC8	pOmniBac-pIDC	Zhang et al., 2017	EDF1, 7, 13
BicDR1-SNAPf	pOmniBac	Urnavicius et al. 2018	F4, EDF13
Lis1-SNAPf	pOmniBac	Elshenawy et al., 2020	F1, 2, 3, 4, EDF1, 2, 3, 4, 5, 6, 7, 8, 9, 11, 12, 13
Lis1 ^{E300K, K303E, S304R, M329A} -SNAPf	pOmniBac	This study	F4, EDF11
Lis1 ^{N203K, D205K, Q222A} -SNAPf	pOmniBac	This study	F4, EDF11
Lis1 ^{M172K, D192K, Y225A, C226D} -SNAPf	pOmniBac	This study	F4, EDF11
Nde1 ¹⁻¹⁹⁰ -SNAPf	pOmniBac	Zhao et al., 2023	F1, 4, EDF1, 2, 7, 11, 13

661

662 **Supplementary Table 1. The list of protein constructs used in this study.** Dynein
663 chains were codon-optimized for *Spodoptera frugiperda* (Sf9) expression and inserted
664 into the pOmniBac backbone. Nde1, Lis1, and BicDR1 constructs were cloned into the
665 pOmniBac backbone. Constructs were tagged with an N-terminal 6xHis-ZZ-TEV site for
666 affinity purification and TEV protease cleavage during protein purification. The SNAPf
667 tag was inserted for labeling the proteins with fluorescent dyes (F: Figure, EDF:
668 Extended Data Figure).

Fig.	Sample	Complex	Expected (kDa)	Measured (kDa)	%	
F 1b	WT Dyn	WT Dyn	1376	1326 ± 49	100*	
	WT Dyn + Lis1 0 min	WT Dyn	1376	1350 ± 65	100*	
	WT Dyn + Lis1 10 min	WT Dyn	1376	1344 ± 55	80*	
		WT Dyn + Lis1	1546	1521 ± 129	20*	
	WT Dyn + Lis1 30 min	WT Dyn	1376	1364 ± 60	65*	
		WT Dyn + Lis1	1546	1544 ± 68	35*	
	WT Dyn + Lis1 60 min	WT Dyn	1376	1359 ± 48	63*	
		WT Dyn + Lis1	1546	1528 ± 40	37*	
	WT Dyn + Lis1 + Nde1 0 min	WT Dyn	1376	1356 ± 64	31*	
WT Dyn + Lis1		1546	1525 ± 70	69*		
WT Dyn + Nde1	WT Dyn	1376	1330 ± 83	100*		
F 4g	WT Lis1	WT Lis1	133	137 ± 17	70	
	Lis1 ^{AAA5}	Lis1 ^{AAA5}	133	141 ± 26	87	
	Lis1 ^{AAA6}	Lis1 ^{AAA6}	133	141 ± 26	87	
	Lis1 ^{Linker}	Lis1 ^{Linker}	133	142 ± 31	90	
	Nde1 ¹⁻¹⁹⁰ + WT Lis1	Nde1 ¹⁻¹⁹⁰		84	85 ± 18	31
		WT Lis1		133	142 ± 15	29
		1 Nde1 ¹⁻¹⁹⁰ + 1 WT Lis1		217	231 ± 20	28
		1 Nde1 ¹⁻¹⁹⁰ + 2 WT Lis1		340	371 ± 44	12
	Nde1 ¹⁻¹⁹⁰ + Lis1 ^{AAA5}	Nde1 ¹⁻¹⁹⁰		84	90 ± 17	37
		Lis1 ^{AAA5}		133	142 ± 13	53
		1 Nde1 ¹⁻¹⁹⁰ + 1 Lis1 ^{AAA5}		217	229 ± 48	10
	Nde1 ¹⁻¹⁹⁰ + Lis1 ^{AAA6}	Nde1 ¹⁻¹⁹⁰		84	82 ± 17	25
		Lis1 ^{AAA6}		133	141 ± 15	30
		1 Nde1 ¹⁻¹⁹⁰ + 1 Lis1 ^{AAA6}		217	233 ± 30	29
		1 Nde1 ¹⁻¹⁹⁰ + 2 Lis1 ^{AAA6}		340	373 ± 16	9
	Nde1 ¹⁻¹⁹⁰ + Lis1 ^{Linker}	Nde1 ¹⁻¹⁹⁰		84	88 ± 16	24
		Lis1 ^{Linker}		133	143 ± 14	26
		1 Nde1 ¹⁻¹⁹⁰ + 1 Lis1 ^{Linker}		217	229 ± 18	30
		1 Nde1 ¹⁻¹⁹⁰ + 2 Lis1 ^{Linker}		340	372 ± 15	12
	F 4h	WT Dyn	WT Dyn	1376	1367 ± 93	100*
WT Dyn + WT Lis1		WT Dyn	1376	1387 ± 52	82*	
		WT Dyn + WT Lis1	1509	1530 ± 39	18*	
WT Dyn + WT Lis1 + Nde1 ¹⁻¹⁹⁰		WT Dyn + WT Lis1	1509	1514 ± 67	100*	
WT Dyn + Lis1 ^{AAA5}		WT Dyn	1376	1367 ± 94	100*	
WT Dyn + Lis1 ^{AAA5} + Nde1 ¹⁻¹⁹⁰		WT Dyn	1376	1361 ± 57	57*	
		WT Dyn + Lis1 ^{AAA5}	1509	1581 ± 76	43*	
WT Dyn + Lis1 ^{AAA6}		WT Dyn	1376	1356 ± 60	100*	
WT Dyn + Lis1 ^{AAA6} + Nde1 ¹⁻¹⁹⁰	WT Dyn	1376	1356 ± 75	77*		
	WT Dyn + 2*Lis1 ^{AAA6} + Nde1 ¹⁻¹⁹⁰		1716	1680 ± 77	23*	

		Nde1 ¹⁻¹⁹⁰			
	WT Dyn + Lis1 ^{Linker}	WT Dyn	1376	1349 ± 56	100 [*]
	WT Dyn + Lis1 ^{Linker} + Nde1 ¹⁻¹⁹⁰	WT Dyn + Lis1 ^{Linker}	1509	1464 ± 75	100 [*]
EDF 1	mtDyn	mtDyn	1376	1362 ± 46	100 [*]
	mtDyn + Lis1 + Nde1	mtDyn	1376	1386 ± 77	32 [*]
		mtDyn + Lis1	1546	1525 ± 74	68 [*]
	mtDyn + Lis1	mtDyn	1376	1411 ± 73	50 [*]
mtDyn + Lis1		1546	1540 ± 57	50 [*]	
EDF 2a	WT Dyn	WT Dyn	1376	1396 ± 241	100 [*]
	WT Dyn + Lis1	WT Dyn	1376	1414 ± 85	100 [*]
	WT Dyn + Nde1	WT Dyn	1376	1371 ± 68	100 [*]
	WT Dyn + Lis1 + Nde1	WT Dyn	1376	1415 ± 85	30 [*]
		WT Dyn + Lis1	1546	1580 ± 63	70 [*]
EDF 2b	WT Dyn	WT Dyn	1376	1347 ± 278	100 [*]
	WT Dyn + Lis1	WT Dyn	1376	1395 ± 167	100 [*]
	WT Dyn + Nde1	WT Dyn	1376	1376 ± 78	100 [*]
	WT Dyn + Lis1 + Nde1	WT Dyn	1376	1391 ± 65	48 [*]
		WT Dyn + Lis1	1546	1585 ± 133	52 [*]
EDF 2c	WT Dyn	WT Dyn	1376	1381 ± 61	100 [*]
	WT Dyn + Lis1	WT Dyn	1376	1371 ± 136	100 [*]
	WT Dyn + Nde1	WT Dyn	1376	1377 ± 113	100 [*]
	WT Dyn + Lis1 + Nde1	WT Dyn	1376	1409 ± 75	45 [*]
		WT Dyn + Lis1	1546	1584 ± 47	55 [*]
EDF 2d	WT Dyn	WT Dyn	1376	1411 ± 108	100 [*]
	WT Dyn + Lis1	WT Dyn	1376	1377 ± 124	100 [*]
	WT Dyn + Nde1	WT Dyn	1376	1366 ± 130	100 [*]
	WT Dyn + Lis1 + Nde1	WT Dyn	1376	1383 ± 56	28 [*]
		WT Dyn + Lis1	1546	1561 ± 51	72 [*]
EDF 2e	WT Dyn	WT Dyn	1376	1396 ± 304	100 [*]
	WT Dyn + Lis1	WT Dyn	1376	1403 ± 76	100 [*]
	WT Dyn + Nde1	WT Dyn	1376	1379 ± 54	100 [*]
	WT Dyn + Lis1 + Nde1	WT Dyn	1376	1402 ± 53	27 [*]
		WT Dyn + Lis1	1546	1581 ± 46	73 [*]

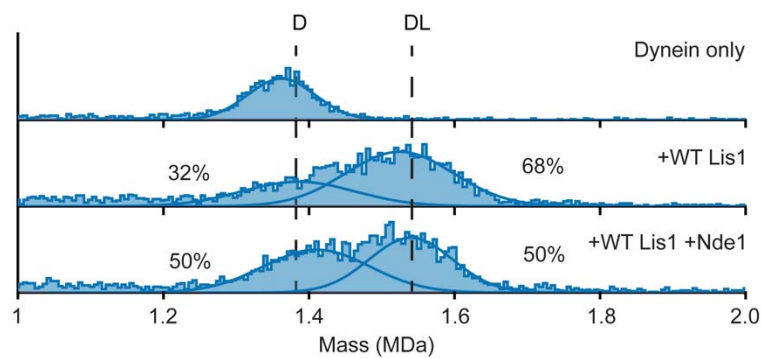
669 **Supplementary Table 2. The parameters of a multi-Gaussian fit of MP**
670 **measurements.** Dynein (Dyn), Lis1, and Nde1 were mixed at 1:2:2 ratio if present and
671 diluted into 5-20 nM. Measured mass and percentage represent the center (mean ± s.d.)
672 and the percent area of the corresponding Gaussian peak (*percentages are normalized
673 so that the sum of all dynein included peaks are 100%). Expected mass corresponds to
674 the dimeric forms of Lis1, Nde1, and Dyn (F: Figure, EDF: Extended Data Figure). Lis1
675 used in F 1b, and EDF 1 contains a ZZ tag, and its expected MW is 170 kDa.

676 **Supplementary Video Legends**

677 **Supplementary Video 1.** Full-length human dynein in Phi^{L} conformation, bound to a
678 Lis1 dimer and displaying the newly identified interface with Lis1.

679 **Supplementary Video 2.** Single-molecule motility recordings of WT DDR complexes, in
680 the presence or absence of Nde1, WT Lis1, and Lis1 mutants. The fluorescence signal
681 originates from BicDR1-mNeonGreen.

682 Extended Data Figures



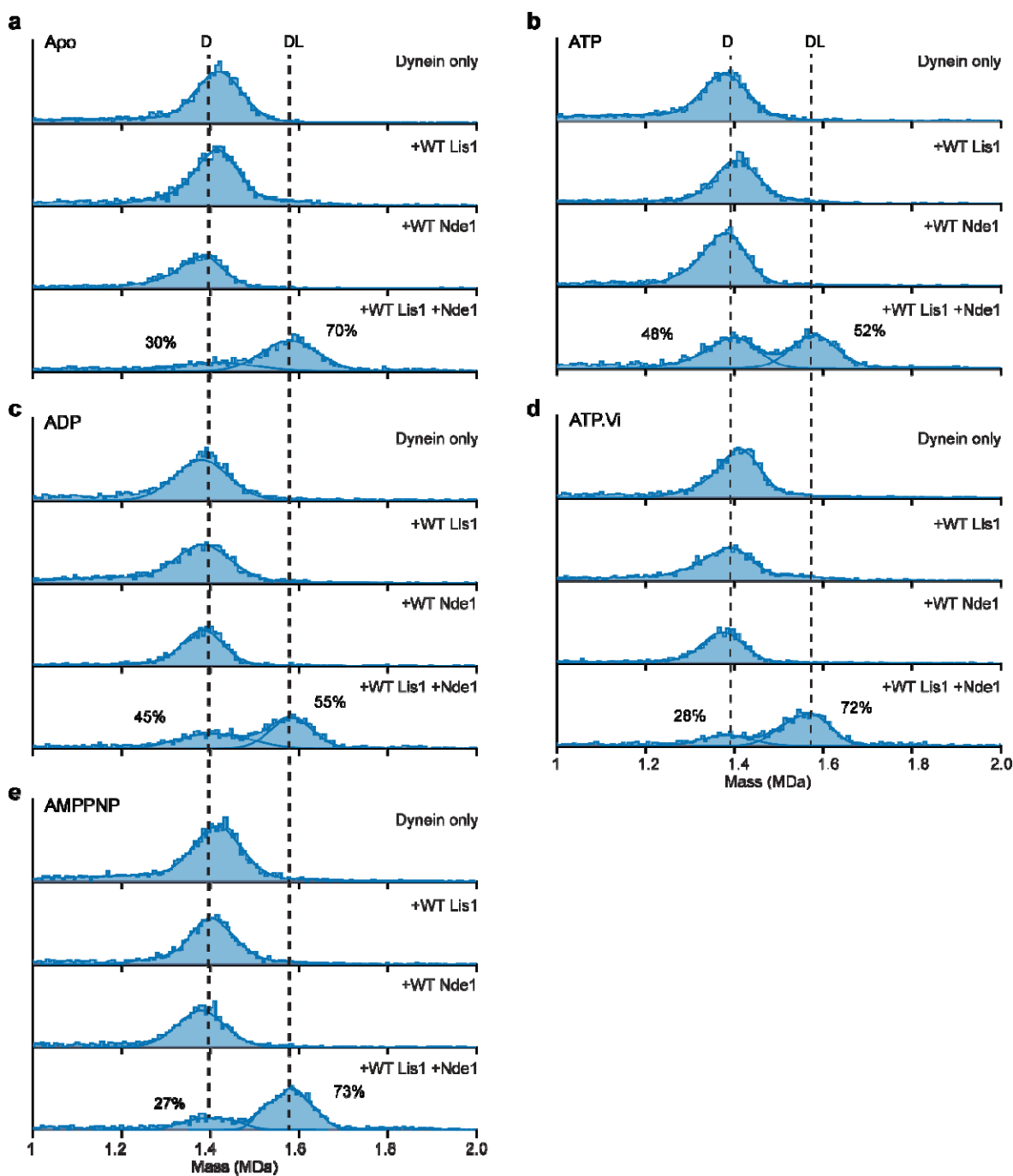
683

684 **Extended Data Fig. 1. MP analysis of Nde1's effect on Lis1 binding to open dynein.**

685 MP shows that Nde1 does not promote increased Lis1 binding to open dynein
686 compared to the Lis1-alone condition, indicating that Lis1 can efficiently bind to open
687 dynein and Nde1 does not enhance Lis1's interaction with open dynein.

688

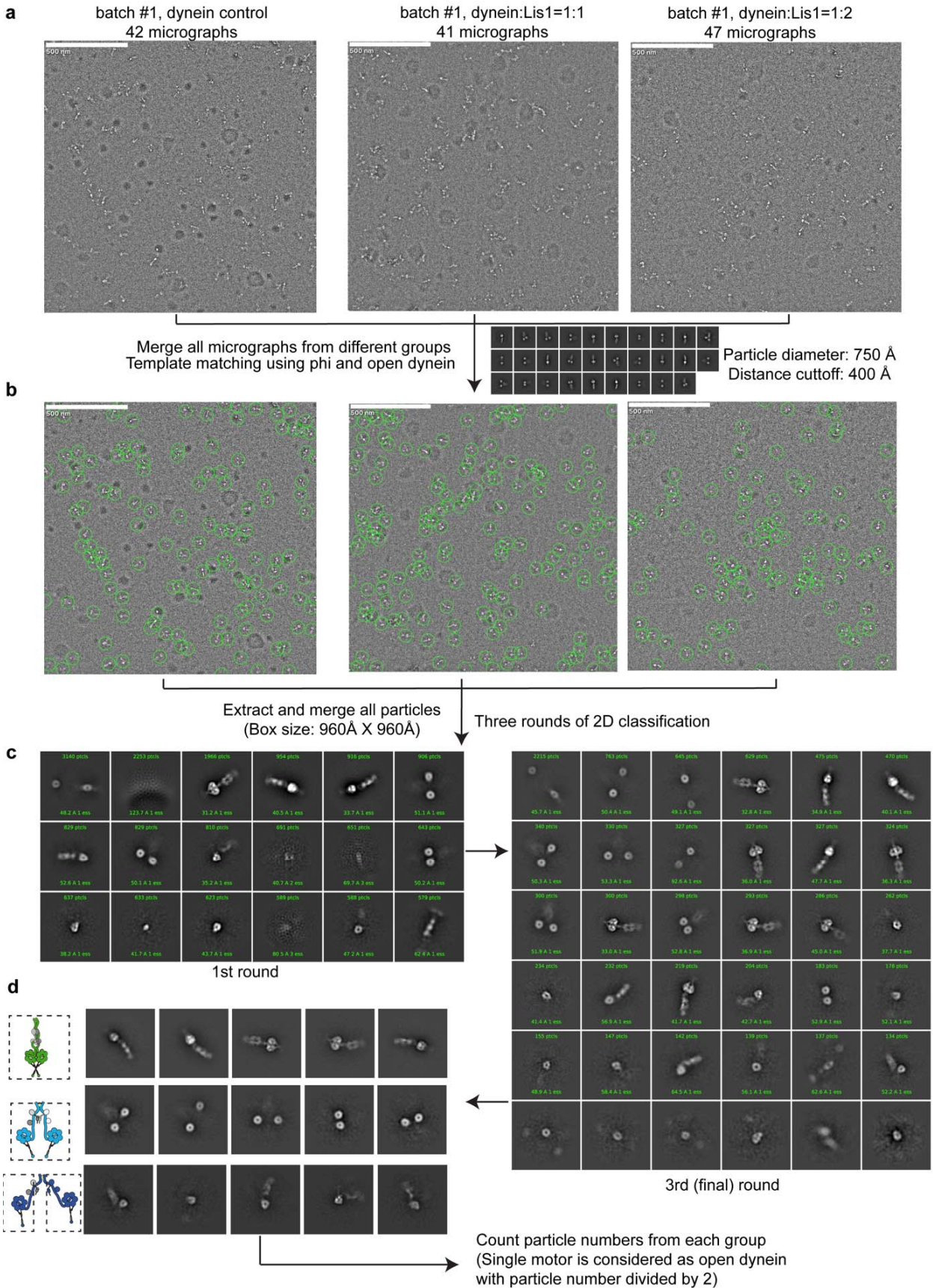
689



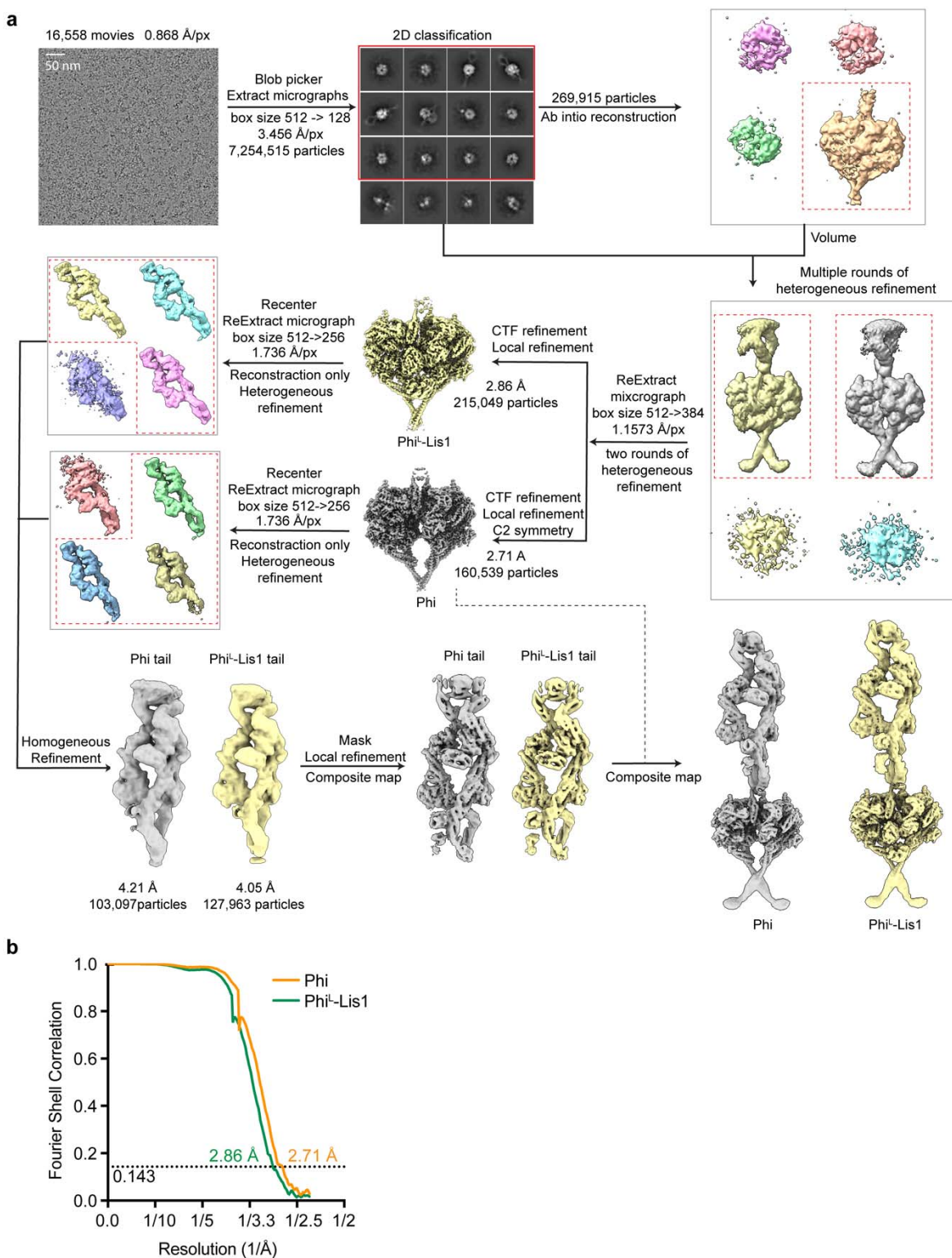
690

691 **Extended Data Fig. 2. MP analysis of nucleotide conditions on Nde1 and Lis1**
692 **binding to WT dynein.** MP shows that under apo buffer (a), 0.1 mM ATP (b), ADP (c),
693 ATP.vi (d), and AMPPNP (e) conditions, Nde1 promotes Lis1 binding to dynein, forming
694 a 1:1 dynein-Lis1 (DL) complex. The nucleotide condition does not affect Nde1's ability
695 to tether Lis1 to dynein. Importantly, the formation of dynein-Nde1, dynein-Lis1-Nde1

696 and 1:2 dynein-Lis1 complexes were not observed. In the Lis1-alone condition, no
697 significant DL complex was formed immediately.

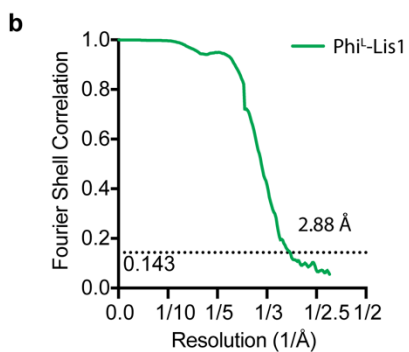
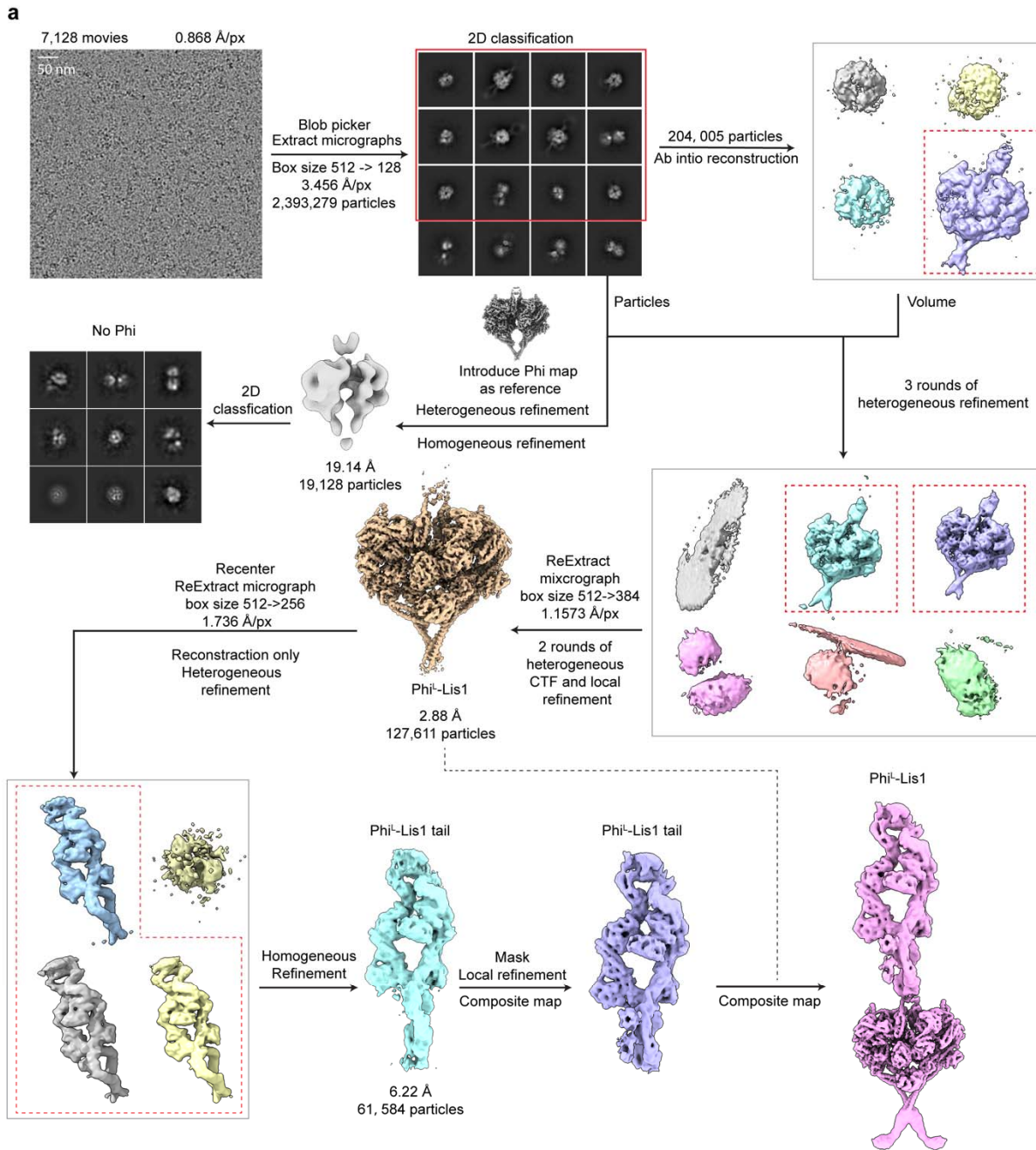


699 **Extended Data Fig. 3. Workflow for negative-stain EM data processing.** **a**,
700 Representative micrographs for dynein alone (42 micrographs), dynein-Lis1 at 1:1 (41
701 micrographs), and dynein-Lis1 at 1:2 (47 micrographs) molar ratios from batch #1. **b**,
702 Particle picking from representative micrographs in each dataset using a template
703 matching approach based on Phi and open dynein models (particle diameter: 750 Å,
704 distance cutoff: 400 Å). **c**, Three rounds of 2D classification were performed after
705 extracting all particles (box size: 960 Å × 960 Å), yielding class averages of Phi dynein,
706 open dynein motors, single motors, and junk particles. **d**, Final classified 2D averages
707 showing Phi dynein, two-motor open dynein, and single-motor open dynein. The particle
708 numbers for each group were counted, and single motors were considered as open
709 dynein by dividing the total number of particles by two.



710
711 **Extended Data Fig. 4. Cryo-EM data processing for the dynein-Lis1 dataset. a, A**
712 **representative cryo-EM micrograph and the flowchart of cryo-EM data processing. b,**

713 Fourier Shell Correlation (FSC) curves showing the final resolution estimates for the
714 motor domains of the Phi (2.71 Å) and Phi^L-Lis1(2.86 Å) datasets.



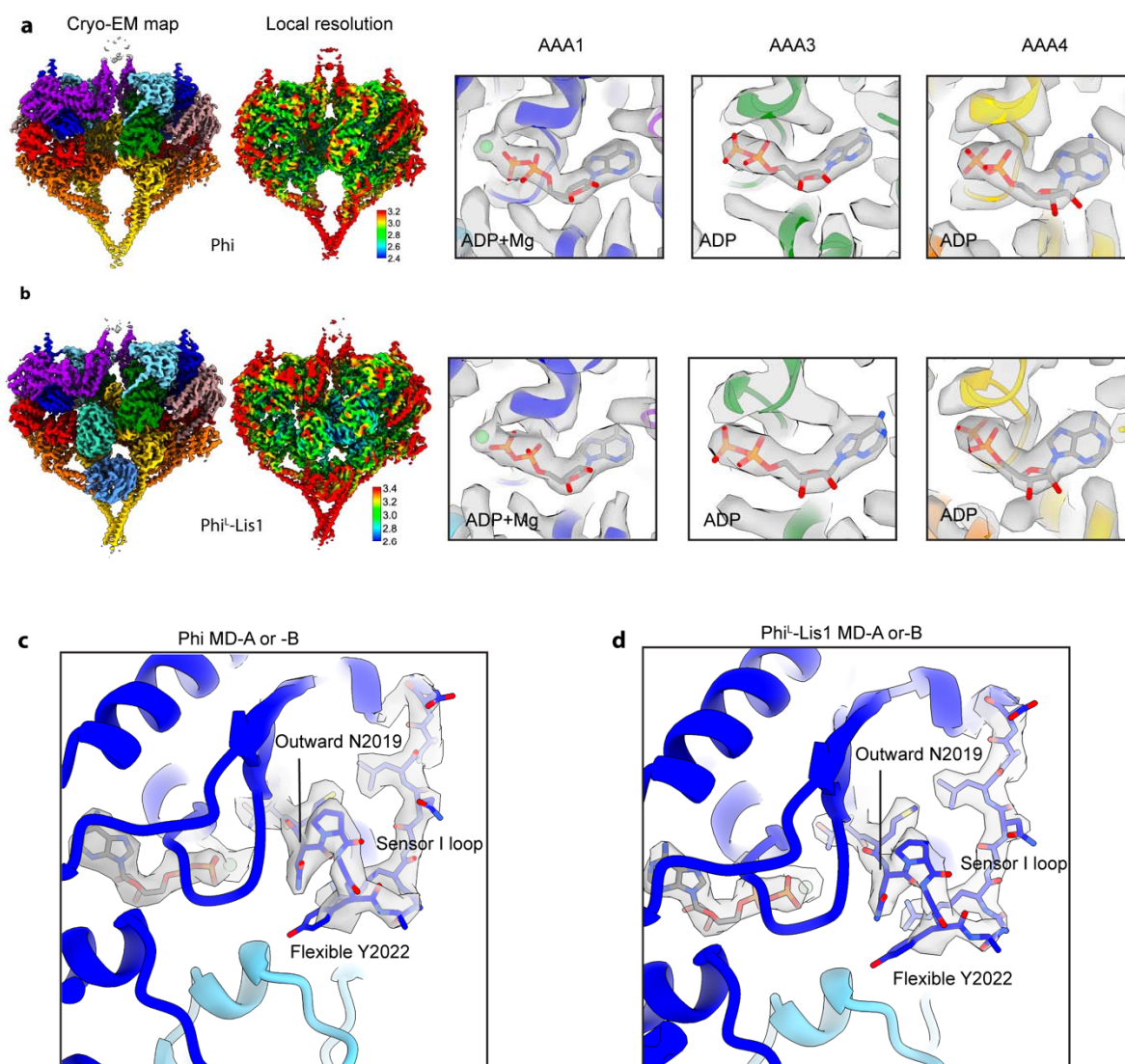
716 **Extended Data Fig. 5. Cryo-EM data processing for the Nde1-Lis1-dynein dataset.**

717 **a**, A representative cryo-EM micrograph and the flowchart of cryo-EM data processing.

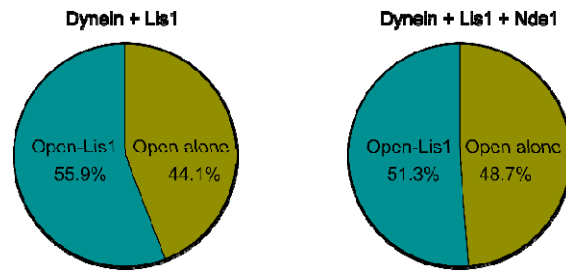
718 **b**, Fourier Shell Correlation (FSC) curve showing the final resolution estimate for the

719 motor domains of the Phi^L-Lis1 (2.88 Å) dataset.

720

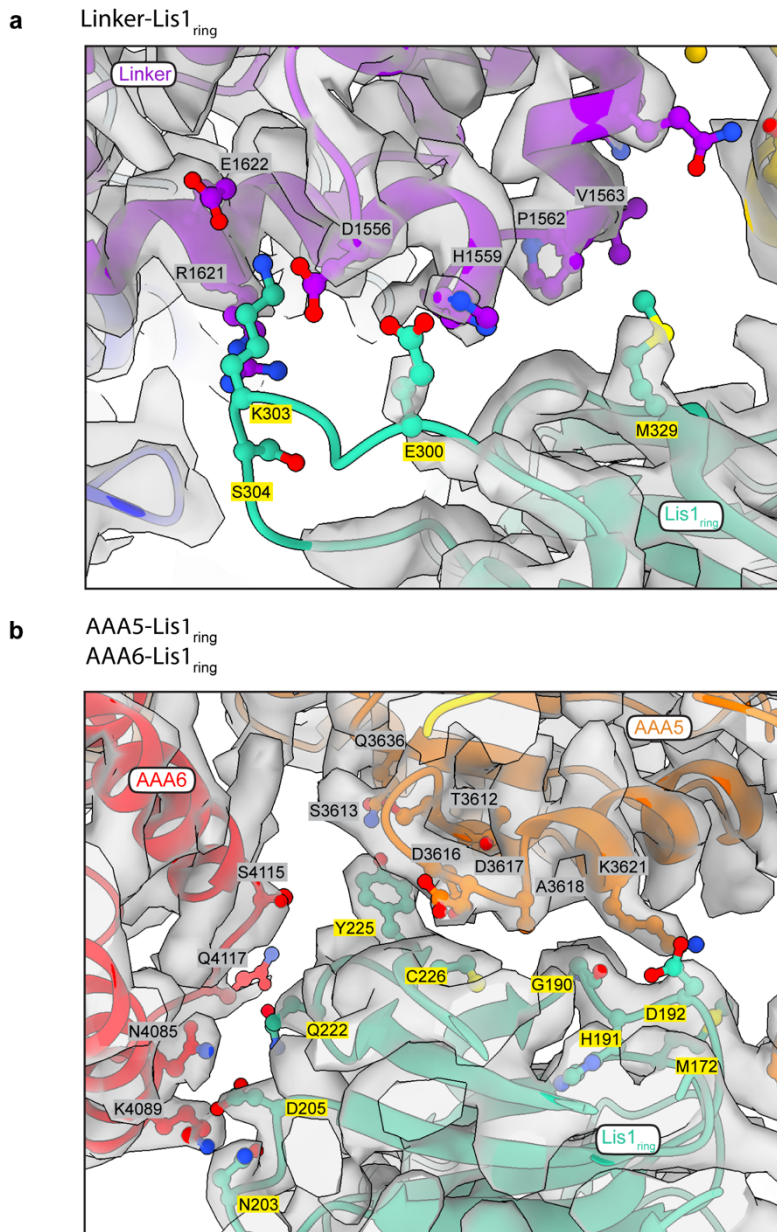


721
722 **Extended Data Fig. 6. Comparison of local resolution, nucleotide binding in AAA1,**
723 **AAA3, AAA4, and sensor-I loop conformation in MD-A of the Phi and Phi^L-Lis1.**
724 Local resolution, and nucleotide binding states in MD-A at AAA1, AAA3, and AAA4 of
725 the Phi (**a**) and Phi^L-Lis1 (**b**). MD-A and -B share the same nucleotide binding in AAA1,
726 AAA3, and AAA4 across both the Phi and Phi^L-Lis1. The sensor-I loop adopts almost
727 the same conformation in MD-A (or -B) of both Phi (**c**) and Phi^L-Lis1 (**d**), indicating that
728 Lis1 binding does not affect phosphate release. The color scheme is the same with Fig.
729 4.

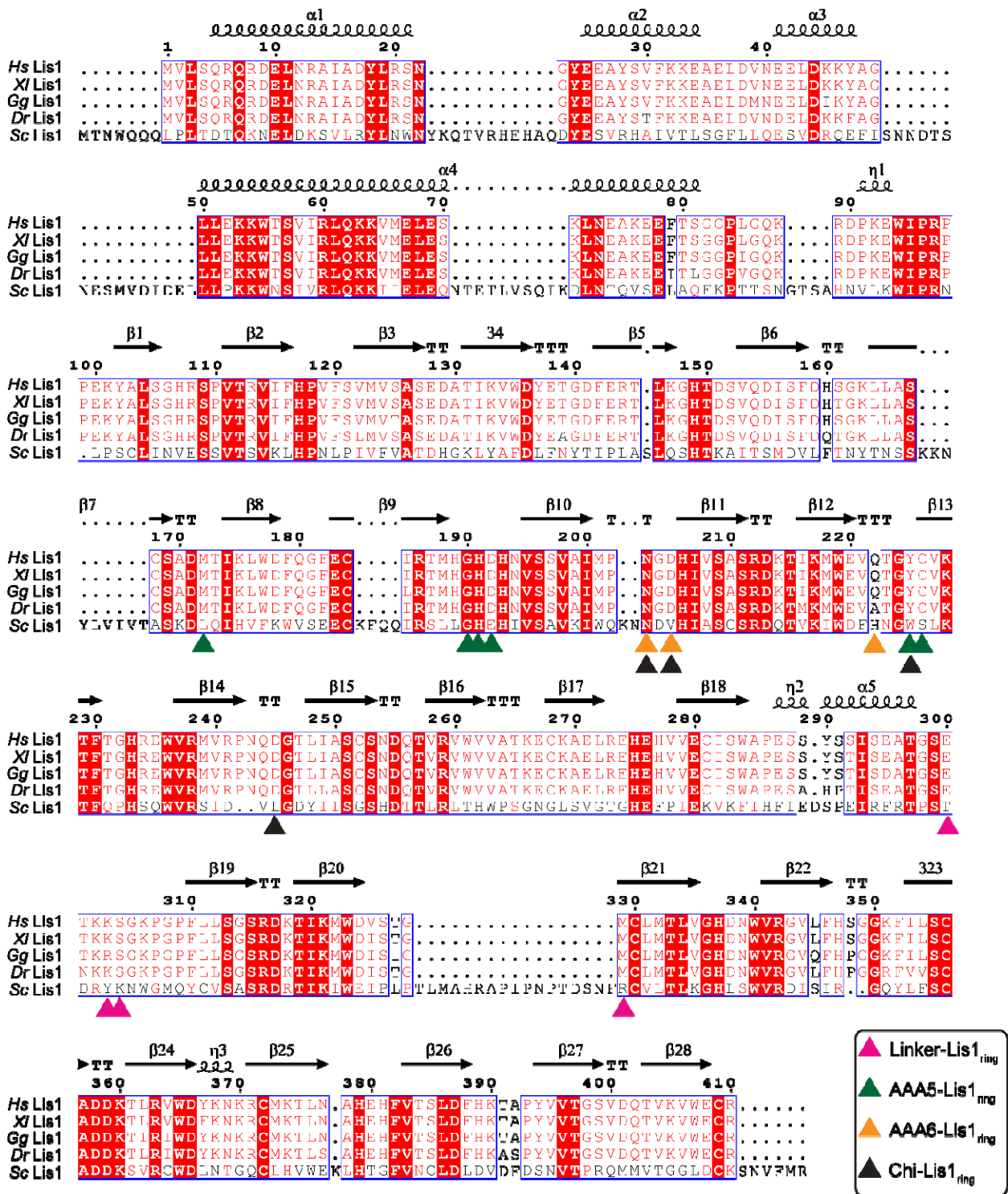


730

731 **Extended Data Fig. 7. Comparison of Nde1's effect on Lis1 binding to the open**
732 **dynein.** The particle numbers for open dynein-Lis1 and open dynein alone were
733 quantified in both the dynein-Lis1 and dynein-Lis1-Nde1 datasets. These results
734 indicate that Nde1 does not promote Lis1 binding to the open dynein motor.



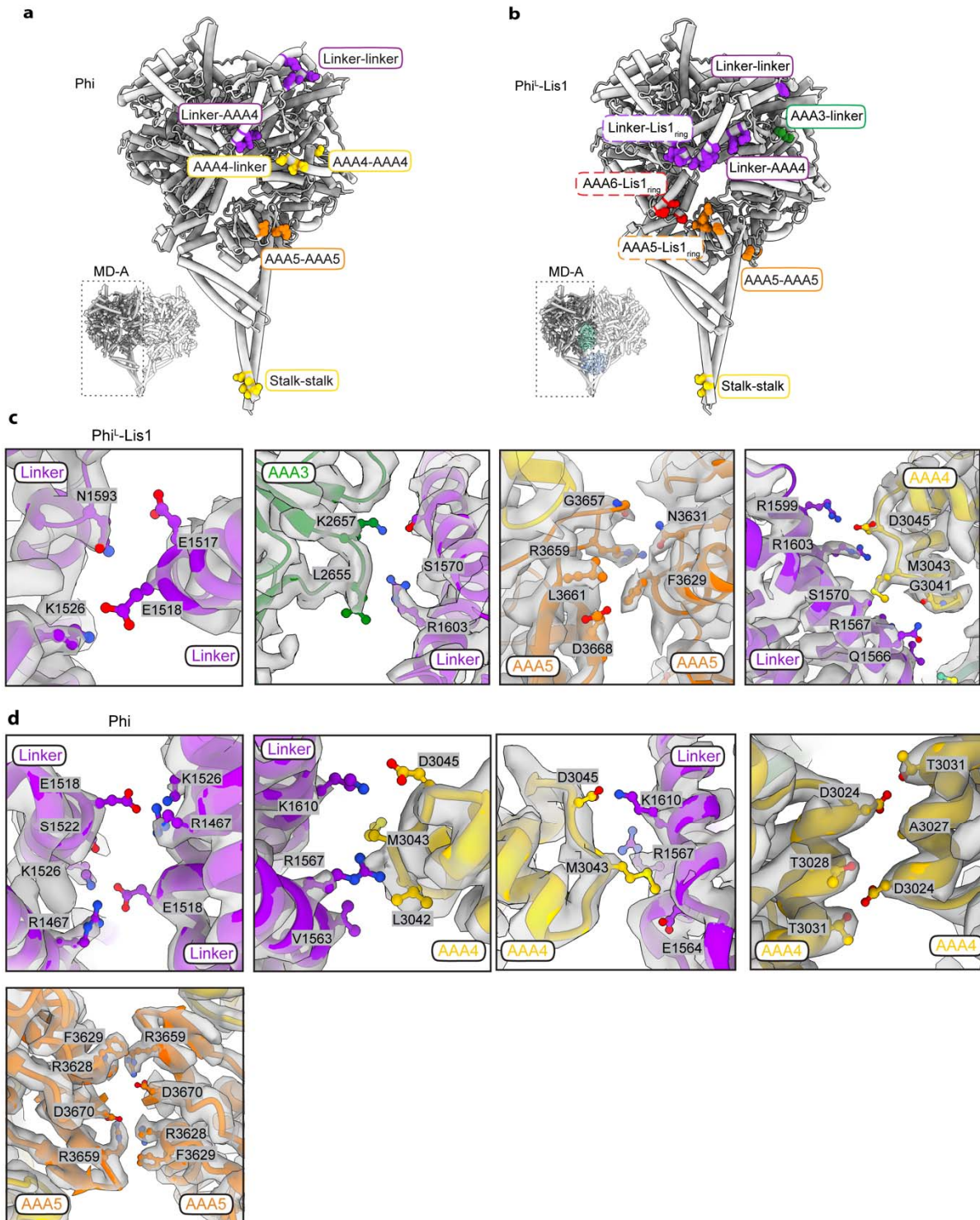
735
736 **Extended Data Fig. 8. Density quality at the dynein MD-A and Lis1 interface in**
737 **Phi^L-Lis1.** **a**, Flexible density at the linker-Lis1_{ring} interface, indicating dynamic
738 interactions in this region. **b**, Well-defined density at the AAA5-Lis1_{ring} and AAA6-Lis1_{ring}
739 regions, showing compact and stable interactions. The color scheme for the motor
740 domains is consistent with Fig. 4.



741
742
743
744
745
746

Extended Data Fig. 9. Sequence alignment of Lis1 homologs among multiple species. Sequence alignment of Lis1 proteins among *Homo sapiens* (Hs Lis1), *Xenopus laevis* (XI Lis1), *Gallus gallus* (Gg Lis1), *Danio rerio* (Dr Lis1), and *Saccharomyces cerevisiae* (Sc Lis1). The secondary structure elements are placed on the top of the alignment. Strictly conserved residues are highlighted in shaded red

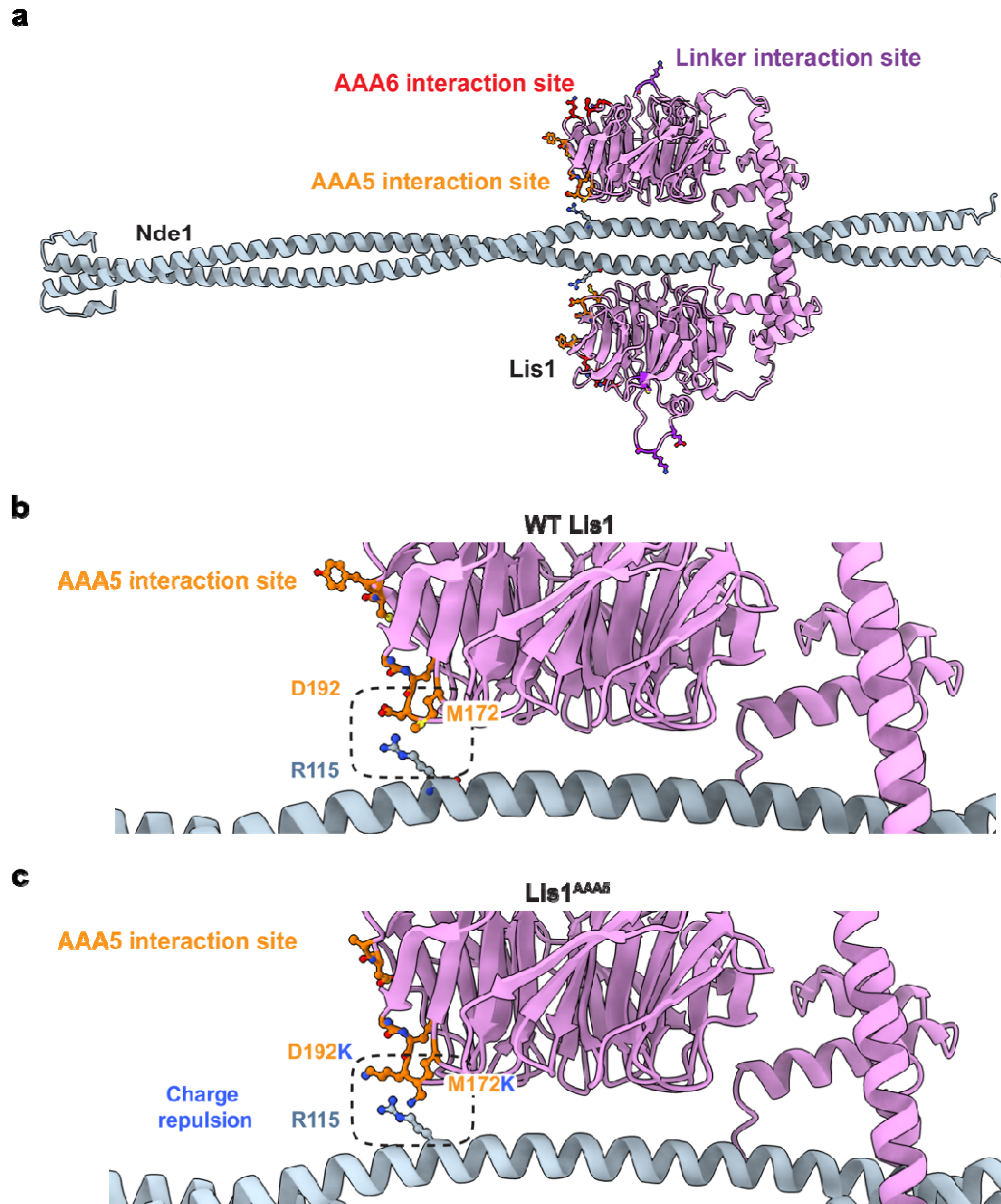
747 boxes, while less-conserved residues are shown in open red boxes. In these open red
748 boxes, red font indicates residues with similar polarity and high conservation, whereas
749 black font represents residues with low similarity. The colored triangles represent key
750 residues involved in interactions at the linker-Lis1_{ring} (purple), AAA5-Lis1_{ring} (green), and
751 AAA6-Lis1_{ring} (orange) interfaces in Phi^L-Lis1. The black triangle represents reported
752 interactions at MD-A and Lis1 interface of modeled human Chi-Lis1 based on the yeast
753 Chi-Lis1³⁷. *S. cerevisiae* Lis1 shows more variation compared to the vertebrate species,
754 suggesting greater evolutionary divergence.



755

756 **Extended Data Fig. 10. Comparison of motor domain A-B interfaces in Phi and**
757 **Phi^L-Lis1. a.** Representative residues located on MD-A that are involved in the MD-A
758 and MD-B interface of Phi, showing interactions at the linker-linker, linker-AAA4, AAA4-
759 linker, AAA4-AAA4, AAA5-AAA5, and stalk-stalk interfaces. **b.** Representative residues

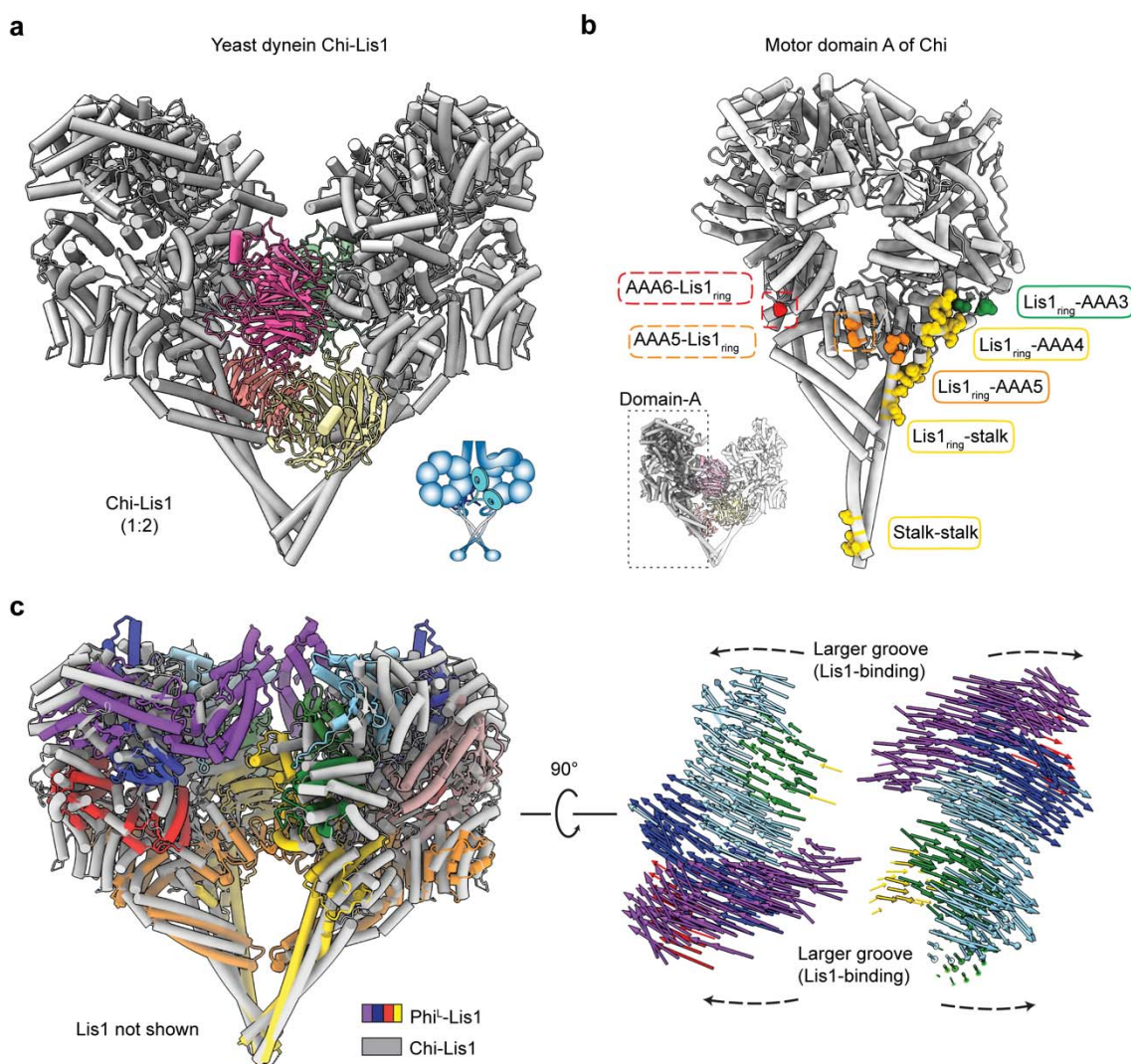
760 located on MD-A of the Phi^{L} -Lis1, involved in the MD-A and Lis1_{ring} interface (including
761 linker-Lis1_{ring}, AAA6-Lis1_{ring}, and AAA5-Lis1_{ring}), and the motor domain A-B interface
762 (including linker-linker, AAA3-linker, linker-AAA4, AAA5-AAA5, and stalk-stalk
763 interfaces). Residues in both panels (a) and (b) are displayed in sphere mode. **c**,
764 Detailed view of the motor domain A-B interface in Phi^{L} -Lis1, showing key residues
765 involved in interactions at the linker-linker, AAA3-linker, AAA5-AAA5, and linker-AAA4
766 interfaces. **d**, Detailed view of motor domain A-B interface of Phi, showing key residues
767 at the linker-linker, linker-AAA4, AAA4-linker, AAA4-AAA4, and AAA5-AAA5 interfaces.



768

769 **Extended Data Fig. 11. Nde1-Lis1 interface predicted by Alphafold.** **a**, Predicted
770 structure of the Nde1-Lis1 complex. Interactions involved in the Phi^{I} MD-A and Lis1
771 interface are shown on the Lis1 surface. **b**, D192 and M172 involved in AAA5-Lis1
772 interface also show contact with R115 of Nde1. **c**, D192K and M172K mutation of
773 Lis1^{AAA5} show charge repulsion with R115 of Nde1. The prediction supports an overlap
774 of the interfaces between the AAA5-Lis1 and Nde1-Lis1.

775



776

777 **Extended Data Fig. 12. Comparison of yeast Chi-Lis1 and human Phi^L-Lis1 motor**
 778 **domains.** **a**, The structure of yeast Chi-Lis1 (PDB:8DZZ)³⁷, showing two tail-truncated
 779 yeast dynein motor domains (grey) bound to two Lis1 dimers (colored, Chi-Lis1 1:2). **b**,
 780 Residues of MD-A that interact with Lis1_{ring} are located in AAA6-Lis1_{ring} and AAA5-
 781 Lis1_{ring} regions and highlighted with dashed rectangle. Representative residues of MD-A
 782 involved in the canonical Lis1_{ring} binding sites are located in Lis1_{ring}-AAA3, Lis1_{ring}-AAA4,
 783 Lis1_{ring}-AAA5 and Lis1_{ring}-stalk region. Interactions between MD-A and MD-B are in
 784 stalk-stalk region. Residues are displayed in sphere mode and are colored according to
 785 the subdomains in Fig. 4. **c**, Superimposition of the human Phi^L-Lis1 and yeast Chi-Lis1
 786 structures, showing that Chi-Lis1 adopts a more expanded conformation, with larger
 787 grooves on both the front and back sides compared to the more compact Phi^L-Lis1

788 structure. Lis1 is hidden for clarity. Vectors represent interatomic distances of pairwise
789 C α atoms between the Phi^L-Lis1 and Chi-Lis1 structures.

790 **Reference**

- 791 1. Reck-Peterson, S.L., Redwine, W.B., Vale, R.D. & Carter, A.P. The cytoplasmic
792 dynein transport machinery and its many cargoes. *Nat Rev Mol Cell Biol* **19**, 382-
793 398 (2018).
- 794 2. McNally, F.J. Mechanisms of spindle positioning. *J Cell Biol* **200**, 131-40 (2013).
- 795 3. Markus, S.M., Marzo, M.G. & McKenney, R.J. New insights into the mechanism
796 of dynein motor regulation by lissencephaly-1. *Elife* **9**(2020).
- 797 4. Willemsen, M.H. et al. Mutations in DYNC1H1 cause severe intellectual disability
798 with neuronal migration defects. *J Med Genet* **49**, 179-83 (2012).
- 799 5. Scoto, M. et al. Novel mutations expand the clinical spectrum of DYNC1H1-
800 associated spinal muscular atrophy. *Neurology* **84**, 668-679 (2015).
- 801 6. Poirier, K. et al. Mutations in TUBG1, DYNC1H1, KIF5C and KIF2A cause
802 malformations of cortical development and microcephaly. *Nat Genet* **45**, 639-47
803 (2013).
- 804 7. Guven, A., Gunduz, A., Bozoglu, T.M., Yalcinkaya, C. & Tolun, A. Novel NDE1
805 homozygous mutation resulting in microhydranencephaly and not
806 microlyssencephaly. *Neurogenetics* **13**, 189-94 (2012).
- 807 8. Lipka, J., Kuijpers, M., Jaworski, J. & Hoogenraad, C.C. Mutations in cytoplasmic
808 dynein and its regulators cause malformations of cortical development and
809 neurodegenerative diseases. *Biochemical Society Transactions* **41**, 1605-1612
810 (2013).
- 811 9. Eschbach, J. & Dupuis, L. Cytoplasmic dynein in neurodegeneration. *Pharmacol*
812 *Ther* **130**, 348-63 (2011).
- 813 10. Urnavicius, L. et al. Cryo-EM shows how dynactin recruits two dyneins for faster
814 movement. *Nature* **554**, 202-206 (2018).
- 815 11. Singh, K. et al. Molecular mechanism of dynein-dynactin complex assembly by
816 LIS1. *Science* **383**, eadk8544 (2024).
- 817 12. Okada, K. et al. Conserved roles for the dynein intermediate chain and Ndel1 in
818 assembly and activation of dynein. *Nature Communications* **14**(2023).
- 819 13. Chaaban, S. & Carter, A.P. Structure of dynein-dynactin on microtubules shows
820 tandem adaptor binding. *Nature* (2022).
- 821 14. Zhang, K. et al. Cryo-EM Reveals How Human Cytoplasmic Dynein Is Auto-
822 inhibited and Activated. *Cell* **169**, 1303-1314 e18 (2017).
- 823 15. Canty, J.T. & Yildiz, A. Activation and Regulation of Cytoplasmic Dynein. *Trends*
824 *in Biochemical Sciences* **45**, 440-453 (2020).
- 825 16. Neuwald, A.F., Aravind, L., Spouge, J.L. & Koonin, E.V. AAA+: A class of
826 chaperone-like ATPases associated with the assembly, operation, and
827 disassembly of protein complexes. *Genome Res* **9**, 27-43 (1999).
- 828 17. Carter, A.P., Cho, C., Jin, L. & Vale, R.D. Crystal Structure of the Dynein Motor
829 Domain. *Science* **331**, 1159-1165 (2011).
- 830 18. Canty, J.T., Tan, R., Kusakci, E., Fernandes, J. & Yildiz, A. Structure and
831 Mechanics of Dynein Motors. *Annu Rev Biophys* **50**, 549-574 (2021).
- 832 19. Chai, P. et al. Cryo-EM Reveals the Mechanochemical Cycle of Reactive Full-
833 length Human Dynein-1. *BioRxiv* (2024).

- 834 20. Cianfrocco, M.A., DeSantis, M.E., Leschziner, A.E. & Reck-Peterson, S.L.
835 Mechanism and regulation of cytoplasmic dynein. *Annu Rev Cell Dev Biol* **31**, 83-
836 108 (2015).
- 837 21. Amos, L.A. Brain dynein crossbridges microtubules into bundles. *J Cell Sci* **93**
838 (**Pt 1**), 19-28 (1989).
- 839 22. Torisawa, T. et al. Autoinhibition and cooperative activation mechanisms of
840 cytoplasmic dynein. *Nature Cell Biology* **16**, 1118+ (2014).
- 841 23. Garrott, S.R., Gillies, J.P. & DeSantis, M.E. Nde1 and Ndel1: Outstanding
842 Mysteries in Dynein-Mediated Transport. *Frontiers in Cell and Developmental*
843 *Biology* **10**(2022).
- 844 24. Bradshaw, N.J., Hennah, W. & Soares, D.C. NDE1 and NDEL1: twin
845 neurodevelopmental proteins with similar 'nature' but different 'nurture'. *Biomol*
846 *Concepts* **4**, 447-64 (2013).
- 847 25. Monda, J.K. & Cheeseman, I.M. Nde1 promotes diverse dynein functions through
848 differential interactions and exhibits an isoform-specific proteasome association.
849 *Molecular Biology of the Cell* **29**, 2336-2345 (2018).
- 850 26. Zhao, Y., Oten, S. & Yildiz, A. Nde1 promotes Lis1-mediated activation of dynein.
851 *Nat Commun* **14**, 7221 (2023).
- 852 27. Shu, T.Z. et al. Ndel1 operates in a common pathway with LIS1 and cytoplasmic
853 dynein to regulate cortical neuronal positioning. *Neuron* **44**, 263-277 (2004).
- 854 28. Stehman, S.A., Chen, Y., McKenney, R.J. & Vallee, R.B. NudE and NudEL are
855 required for mitotic progression and are involved in dynein recruitment to
856 kinetochores. *Journal of Cell Biology* **178**, 583-594 (2007).
- 857 29. Wang, S.S. et al. Nudel/NudE and Lis1 promote dynein and dynactin interaction
858 in the context of spindle morphogenesis. *Molecular Biology of the Cell* **24**, 3522-
859 3533 (2013).
- 860 30. McKenney, R.J., Vershinin, M., Kunwar, A., Vallee, R.B. & Gross, S.P. LIS1 and
861 NudE Induce a Persistent Dynein Force-Producing State. *Cell* **141**, 304-314
862 (2010).
- 863 31. Reiner, O. & Sapir, T. LIS1 functions in normal development and disease.
864 *Current Opinion in Neurobiology* **23**, 951-956 (2013).
- 865 32. Huang, J., Roberts, A.J., Leschziner, A.E. & Reck-Peterson, S.L. Lis1 Acts as a
866 "Clutch" between the ATPase and Microtubule-Binding Domains of the Dynein
867 Motor. *Cell* **150**, 975-986 (2012).
- 868 33. Qiu, R.D., Zhang, J. & Xiang, X. LIS1 regulates cargo-adaptor-mediated
869 activation of dynein by overcoming its autoinhibition in vivo. *Journal of Cell*
870 *Biology* **218**, 3630-3646 (2019).
- 871 34. Elshenawy, M.M. et al. Lis1 activates dynein motility by modulating its pairing
872 with dynactin. *Nat Cell Biology* **22**, 570-578 (2020).
- 873 35. Htet, Z.M. et al. LIS1 promotes the formation of activated cytoplasmic dynein-1
874 complexes. *Nature Cell Biology* **22**, 518+ (2020).
- 875 36. McKenney, R.J. LIS1 cracks open dynein. *Nature Cell Biology* **22**, 515-517
876 (2020).
- 877 37. Karasmanis, E.P. et al. Lis1 relieves cytoplasmic dynein-1 autoinhibition by
878 acting as a molecular wedge. *Nat Struct Mol Biol* **30**, 1357-1364 (2023).

- 879 38. Ton, W.D. et al. Microtubule-binding-induced allostery triggers LIS1 dissociation
880 from dynein prior to cargo transport. *Nature Structural & Molecular Biology*
881 (2023).
- 882 39. Kusakci, E. et al. Lis1 slows force-induced detachment of cytoplasmic dynein
883 from microtubules. *Nature Chemical Biology* **20**(2024).
- 884 40. Neer, E.J., Schmidt, C.J., Nambudripad, R. & Smith, T.F. The ancient regulatory-
885 protein family of WD-repeat proteins. *Nature* **371**, 297-300 (1994).
- 886 41. Emes, R.D. & Ponting, C.P. A new sequence motif linking lissencephaly,
887 Treacher Collins and oral-facial-digital type 1 syndromes, microtubule dynamics
888 and cell migration. *Hum Mol Genet* **10**, 2813-20 (2001).
- 889 42. Mateja, A., Cierpicki, T., Paduch, M., Derewenda, Z.S. & Otlewski, J. The
890 dimerization mechanism of LIS1 and its implication for proteins containing the
891 LisH motif. *Journal of Molecular Biology* **357**, 621-631 (2006).
- 892 43. Reimer, J.M., DeSantis, M.E., Reck-Peterson, S.L. & Leschziner, A.E. Structures
893 of human dynein in complex with the lissencephaly 1 protein, LIS1. *Elife*
894 **12**(2023).
- 895 44. Marzo, M.G., Griswold, J.M. & Markus, S.M. Pac1/LIS1 stabilizes an uninhibited
896 conformation of dynein to coordinate its localization and activity. *Nature Cell*
897 *Biology* **22**, 559-+ (2020).
- 898 45. Geohring, I.C. et al. A nucleotide code governs Lis1's ability to relieve dynein
899 autoinhibition. *bioRxiv* (2024).
- 900 46. Wynne, C.L. & Vallee, R.B. Cdk1 phosphorylation of the dynein adapter Nde1
901 controls cargo binding from G2 to anaphase. *Journal of Cell Biology* **217**, 3019-
902 3029 (2018).
- 903 47. Lam, C., Vergnolle, M.A., Thorpe, L., Woodman, P.G. & Allan, V.J. Functional
904 interplay between LIS1, NDE1 and NDEL1 in dynein-dependent organelle
905 positioning. *J Cell Sci* **123**, 202-12 (2010).
- 906 48. Zhang, Y.F. et al. Nde1 is a Rab9 effector for loading late endosomes to
907 cytoplasmic dynein motor complex. *Structure* **30**, 386-+ (2022).
- 908 49. Doobin, D.J., Helmer, P., Carabalona, A., Bertipaglia, C. & Vallee, R.B. The Role
909 of Nde1 phosphorylation in interkinetic nuclear migration and neural migration
910 during cortical development. *Mol Biol Cell* **35**, ar129 (2024).
- 911 50. Pei, Z. et al. The Expression and Roles of Nde1 and Ndel1 in the Adult
912 Mammalian Central Nervous System. *Neuroscience* **271**, 119-136 (2014).
- 913 51. Derewenda, U. et al. The structure of the coiled-coil domain of Ndel1 and the
914 basis of its interaction with Lis1, the causal protein of Miller-Dieker lissencephaly.
915 *Structure* **15**, 1467-81 (2007).
- 916 52. Garrott, S.R. et al. Ndel1 disfavors dynein-dynactin-adaptor complex formation in
917 two distinct ways. *J Biol Chem* **299**, 104735 (2023).
- 918 53. Ye, F. et al. DISC1 Regulates Neurogenesis via Modulating Kinetochores
919 Attachment of Ndel1/Nde1 during Mitosis. *Neuron* **96**, 1204 (2017).
- 920 54. McKenney, R.J., Weil, S.J., Scherer, J. & Vallee, R.B. Mutually Exclusive
921 Cytoplasmic Dynein Regulation by NudE-Lis1 and Dynactin. *Journal of Biological*
922 *Chemistry* **286**, 39615-39622 (2011).

- 923 55. Nyarko, A., Song, Y.J. & Barbar, E. Intrinsic Disorder in Dynein Intermediate
924 Chain Modulates Its Interactions with NudE and Dynactin. *Journal of Biological*
925 *Chemistry* **287**, 24884-24893 (2012).
- 926 56. Moon, H.M. et al. LIS1 controls mitosis and mitotic spindle organization via the
927 LIS1-NDEL1-dynein complex. *Hum Mol Genet* **23**, 449-66 (2014).
- 928 57. Zylkiewicz, E. et al. The N-terminal coiled-coil of Ndel1 is a regulated scaffold
929 that recruits LIS1 to dynein. *J Cell Biol* **192**, 433-45 (2011).
- 930 58. Wang, S.S. & Zheng, Y.X. Identification of a novel dynein binding domain in
931 nudel essential for spindle pole organization in Xenopus egg extract. *Journal of*
932 *Biological Chemistry* **286**, 587-593 (2011).
- 933 59. Efimov, V.P. Roles of NUDE and NUDF Proteins of *Aspergillus nidulans*: Insights
934 from Intracellular Localization and Overexpression Effects. *Molecular Biology of*
935 *the Cell* **14**, 871-888 (2003).
- 936 60. Toropova, K. et al. Lis1 regulates dynein by sterically blocking its
937 mechanochemical cycle. *Elife* **3**(2014).
- 938 61. Cianfrocco, M.A. et al. Lis1 has Two Distinct Modes of Regulating Dynein's
939 Mechanochemical Cycle. *Biophysical Journal* **112**, 43a-43a (2017).
- 940 62. Gillies, J.P. et al. Structural basis for cytoplasmic dynein-1 regulation by Lis1.
941 *Elife* **11**(2022).
- 942 63. Schlager, M.A., Hoang, H.T., Urnavicius, L., Bullock, S.L. & Carter, A.P. In vitro
943 reconstitution of a highly processive recombinant human dynein complex. *EMBO*
944 *J* **33**, 1855-68 (2014).
- 945 64. Urnavicius, L. et al. The structure of the dynactin complex and its interaction with
946 dynein. *Science* **347**, 1441-1446 (2015).
- 947 65. Casanal, A., Lohkamp, B. & Emsley, P. Current developments in Coot for
948 macromolecular model building of Electron Cryo-microscopy and
949 Crystallographic Data. *Protein Sci* **29**, 1069-1078 (2020).
- 950 66. Kidmose, R.T. et al. Namdinator - automatic molecular dynamics flexible fitting of
951 structural models into cryo-EM and crystallography experimental maps. *IUCrJ* **6**,
952 526-531 (2019).
- 953 67. Afonine, P.V. et al. Real-space refinement in PHENIX for cryo-EM and
954 crystallography. *Acta Crystallogr D Struct Biol* **74**, 531-544 (2018).

955